ALMA MATER STUDIORUM
UNIVERSITÀ DI BOLOGNA

DIPARTIMENTO DI INGEGNERIA INDUSTRIALE

CORSO DI LAUREA MAGISTRALE IN
INGEGNERIA ENERGETICA

DESTABILIZATION AND CHARACTERIZATION OF TOROIDICITY-INDUCED ALFVÉN EIGENMODES WITH GYSELA

Relatore

Prof. Mostacci Domiziano

Correlatore

Mazzi Samuele

Presentata da

Lorenzo Bramucci

Sessione luglio 2024

Anno Accademico 2023/2024

ALMA MATER STUDIORUM
UNIVERSITÀ DI BOLOGNA

DIPARTIMENTO DI INGEGNERIA INDUSTRIALE

CORSO DI LAUREA MAGISTRALE IN
INGEGNERIA ENERGETICA

DESTABILIZATION AND CHARACTERIZATION OF TOROIDICITY-INDUCED ALFVÉN EIGENMODES WITH GYSELA

Relatore

Prof. Domiziano Mostacci

Correlatore

Samuele Mazzi

Presentata da

Lorenzo Bramucci

Sessione luglio 2024

Anno Accademico 2023/2024

Abstract

La fusione nucleare rappresenta una promettente soluzione alla crescente domanda di energia del mondo, offrendo una fonte energetica pulita e virtualmente illimitata. Questa tesi si concentra sulla fusione a confinamento magnetico nei tokamak, ovvero dispositivi che utilizzano forti campi magnetici per confinare il plasma caldo in una forma toroidale. Il design del tokamak è particolarmente efficace poiché consente di creare un ambiente di plasma stabile in cui possono avvenire le reazioni di fusione. La fusione tra deuterio e trizio (fusione D-T) è la reazione attualmente più fattibile e studiata e produce una quantità significativa di energia. Nella reazione di fusione D-T, i nuclei di deuterio e trizio si combinano per formare un nucleo di elio (detto anche particella alfa) e un neutrone ad alta energia. Le particelle alfa, che data la loro energia sono ioni veloci, svolgono un ruolo cruciale nel riscaldamento del plasma e nel mantenimento della sua temperatura. Queste particelle, prodotte durante le reazioni di fusione, devono essere confinate in modo efficace per trasferire la loro energia nel plasma, mantenendo così le alte temperature necessarie per le reazioni di fusione. La capacità di confinare le particelle alfa è essenziale per ottenere una reazione di fusione autosufficiente, nota come “ignition” (accensione), in cui l’energia generata dalle reazioni di fusione è sufficiente a sostenere il plasma senza riscaldamento esterno.

Oltre alle particelle alfa prodotte direttamente dalle reazioni di fusione, gli ioni veloci sono generati anche da sistemi di riscaldamento esterni, come il Neutral Beam Injection (NBI), che utilizza l’iniezione di fasci di neutri o l’ Ion Cyclotron Resonance Heating (ICRH), che utilizza la risonanza ciclotrononica degli ioni. Questi sistemi iniettano ioni ad alta energia nel plasma per contribuire a raggiungere e sostenere le temperature estremamente elevate necessarie per le reazioni di fusione. Il comportamento di questi ioni veloci è fondamentale per l’efficienza e la stabilità del plasma, in quanto forniscono il necessario riscaldamento e le correnti di pilotaggio all’interno del plasma. Tuttavia, l’interazione tra gli ioni veloci e le onde del plasma, come gli Alfvén eigenmode, può portare a instabilità che rappresentano una sfida significativa per mantenere il confinamento del plasma e ottenere reazioni di fusione continue.

Le onde di Alfvén sono oscillazioni a bassa frequenza in un plasma magnetizzato, dove ioni e campi magnetici interagiscono, propagandosi lungo le linee del campo magnetico e spinte dalla tensione del campo magnetico, proprio come le onde su una corda tesa. Gli Alfvén Eignemodes sono modelli di oscillazione naturali (eignemode) delle onde di Alfvén all’interno di un sistema di plasma confinato, come un tokamak, che rappresentano stati oscillatori specifici e stabili del plasma, determinati dalla geometria del sistema e dalla configurazione del campo magnetico. Gli Alfvén Eignemodes indotti dalla toroidicità (Toroidal Alfvèn Eignemode-TAE) sono un sottoinsieme di autovalori di Alfvén che nascono specificamente a causa della geometria toroidale dei tokamak; la curvatura e la diversa intensità del campo magnetico attorno al toro modificano le onde di Alfvén, creando questi autovalori distinti. I TAE sono importanti perché possono entrare in risonanza con gli ioni veloci, portando potenzialmente a instabilità che possono influenzare il confinamento e le prestazioni del plasma. Lo studio di queste interazioni è fondamentale per prevedere e mitigare i loro effetti negativi nei dispositivi di fusione.

Il codice GYSELA, utilizzato in questo lavoro, è un codice avanzato di simulazione semilagrangiana girocinetica specificamente progettato per modellare la dinamica del plasma nei tokamak. Utilizza tecniche numeriche sofisticate per simulare il comportamento delle particelle di plasma e le loro interazioni con i campi elettromagnetici all'interno di geometrie simili a quelle dei tokamak. Le capacità di GYSELA si estendono allo studio della stabilità, del confinamento e delle proprietà di trasporto del plasma, cruciali per l'ottimizzazione dei futuri reattori a fusione. Le sue simulazioni forniscono una visione dettagliata della complessa fisica dei plasmi ad alta temperatura, contribuendo allo sviluppo di tecnologie energetiche di fusione più efficienti e affidabili. GYSELA offre quindi un potente strumento di simulazione per studiare la dinamica non lineare dei TAE e le loro interazioni con gli ioni veloci nei plasmi toroidali.

Il primo passo è stato quello di caratterizzare gli autovalori di Alfvén in una configurazione cilindrica per studiare questi fenomeni. Questo modello semplificato ha permesso di comprendere nel dettaglio le proprietà fondamentali e il comportamento degli Alfvén Eignemodes senza l'aggiunta della complessità della geometria toroidale. Analizzando a fondo questi modi in una configurazione cilindrica, sono state acquisite conoscenze essenziali sulla loro eccitazione e interazione con gli ioni veloci, costituendo una base per simulazioni più complesse.

Successivamente, sono state effettuate analisi in una configurazione toroidale, più realistica, per esaminare i TAEs. Per studiare l'interazione tra ioni veloci e TAE è stata utilizzata un'antenna elettrostatica per perturbare il plasma. Questo metodo consente un'eccitazione controllata dei TAE, permettendo di esaminare come gli ioni veloci influenzano questi modi. L'uso di un'antenna elettrostatica è fondamentale perché fornisce un mezzo riproducibile e regolabile per eccitare modi specifici all'interno del plasma, facilitando misure precise ed esperimenti controllati. Integrando questa tecnica nelle simulazioni di GYSELA, lo studio fornisce un'analisi preliminare dei meccanismi attraverso i quali gli ioni veloci destabilizzano i TAE e il conseguente impatto sulla stabilità e sul confinamento del plasma.

Abstract

Nuclear fusion stands as a promising solution to the world's growing energy demands, offering a clean and virtually limitless energy source. This thesis focuses on magnetic confinement fusion in tokamak devices, which use strong magnetic fields to confine hot plasma in a toroidal shape. The tokamak design is particularly effective because it allows for the creation of a stable plasma environment where fusion reactions can occur. The fusion of deuterium and tritium (D-T fusion) is the most feasible reaction for current fusion research, producing a significant amount of energy. In a D-T fusion reaction, the nuclei of deuterium and tritium combine to form a helium nucleus (alpha particle) and a high-energy neutron. The alpha particles, which are fast ions, play a crucial role in heating the plasma and maintaining its temperature. These particles, produced during the fusion reactions, must be effectively confined to transfer their energy back into the plasma, thereby maintaining the high temperatures necessary for ongoing fusion reactions. The ability to confine alpha particles is essential for achieving a self-sustaining fusion reaction, known as ignition, where the energy generated from the fusion reactions is sufficient to sustain the plasma without external heating.

In addition to alpha particles produced directly from the fusion reactions, fast ions are also generated by external heating systems, such as neutral beam injection (NBI) and ion cyclotron resonance heating (ICRH). These systems inject high-energy ions into the plasma to help achieve and sustain the extremely high temperatures required for fusion reactions. The behaviour of these fast ions is critical for the efficiency and stability of the plasma, as they provide the necessary heating and drive currents within the plasma. However, the interaction between fast ions and plasma waves, such as Alfvén eigenmodes, can lead to instabilities that pose significant challenges for maintaining plasma confinement and achieving continuous fusion reactions.

Alfvén waves are low-frequency oscillations in a magnetized plasma, where ions and magnetic fields interact, propagating along the magnetic field lines and driven by the tension in the magnetic field, much like waves on a stretched string. Alfvén eigenmodes are natural oscillation patterns (eigenmodes) of Alfvén waves within a confined plasma system, such as a tokamak, representing specific, stable oscillatory states of the plasma, determined by the system's geometry and magnetic field configuration. Toroidicity-induced Alfvén Eigenmodes (TAEs) are a subset of Alfvén eigenmodes that arise specifically due to the toroidal geometry of tokamak devices; the curvature and the varying magnetic field strength around the torus modify the Alfvén waves, creating these distinct eigenmodes. TAEs are significant because they can resonate with the fast ions, potentially leading to instabilities that can affect the plasma confinement and performance. Studying these interactions is vital for predicting and mitigating their adverse effects in fusion devices.

The GYSELA code, utilized in this work, is an advanced gyrokinetic semi-Lagrangian simulation code specifically designed to model toroidal plasma dynamics. It utilizes sophisticated numerical techniques to simulate the behaviour of plasma particles and their interactions with electromagnetic fields within tokamak-like geometries. GYSELA's capabilities extend to studying the stability, confinement, and transport properties of plasma, crucial for optimizing

fusion reactor performance. Its simulations provide detailed insights into the complex physics of high-temperature plasmas, contributing to the development of more efficient and reliable fusion energy technologies. Thus GYSELA offers a powerful simulation tool for investigating the nonlinear dynamics of TAEs and their interactions with fast ions in toroidal plasmas.

The first step involved characterizing Alfvén eigenmodes in a cylindrical configuration to study these phenomena. This simplified model allowed for a detailed understanding of the fundamental properties and behaviour of Alfvén eigenmodes without the added complexity of toroidal geometry. By thoroughly analyzing these modes in a cylindrical setup, essential insights were gained into their excitation and interaction with fast ions, forming a foundation for more complex simulations.

Subsequently, analyses were carried out in a more realistic toroidal configuration to examine the TAEs. To investigate the interaction between fast ions and TAEs an electrostatic antenna was used to perturb the plasma. This method allows for a controlled excitation of TAEs, enabling an examination of how fast ions influence these modes. The use of an electrostatic antenna is crucial because it provides a reproducible and adjustable means of exciting specific modes within the plasma, facilitating precise measurements and controlled experiments. By integrating this technique within the GYSELA simulations, the study provides a preliminary analysis of the mechanisms through which fast ions destabilize TAEs and the resulting impact on plasma stability and confinement.

Table of Contents

List of Figures

Chapter 1

Inroduction to Plasma Physics

This chapter presents an overview of nuclear fusion, the reaction involved, the magnetically confined plasma, the motion of charged particles in a magnetic field and some models to describe the plasma. It focuses in particular on the gyrokinetic theory, which is the one that is used in GYSELA, the numerical code for plasma core simulation has been used in this work. Finally, it briefly introduces the instabilities in a tokamak, with a more detailed investigation on the Alfvén Waves in fusion plasmas, which are the main focus of this thesis.
This thesis was carried out during the internship at the Institute de la Recherche sure la Fusion par confinment Magnetiqué, an institute of CEA, the French Alternatives Energies and Atomic Energy Commission, located in the CEA Cadarache center located in the south of France.

1.1 Nuclear fusion

One of the greatest challenges facing our society today is the energy transition. To achieve this, it is crucial to find sustainable, carbon-free sources of energy. With this in mind, magnetically controlled thermonuclear fusion is an ideal candidate for reaching this goal. This energy source relies on the nuclear fusion reaction between light atom nuclei to release energy.

A nuclei with atomic mass A has Z protons and N neutrons kept together by a binding Energy Δ. The higher the ratio Δ/A is, the more stable is the nucleus. Figure 1.1 represents the binding energy of nucleons in atom nuclei and it is possible to observe that the most stable element, the one with the highest ratio Δ/A, is Iron with atomic mass A of 56. When nuclear reactions lead to the production of nuclei that are more stable than the initial ones they release energy and are considered exothermic. In such reactions, the total mass of the reactants is higher than that of the products and the energy released during the process is equivalent to the mass defect associated with the reaction.

It can be observed that for elements with an atomic number lower than the Iron one, it is energetically convenient to initiate fusion processes, whereas, for those with a higher atomic number, it is energetically favourable to initiate fission processes.

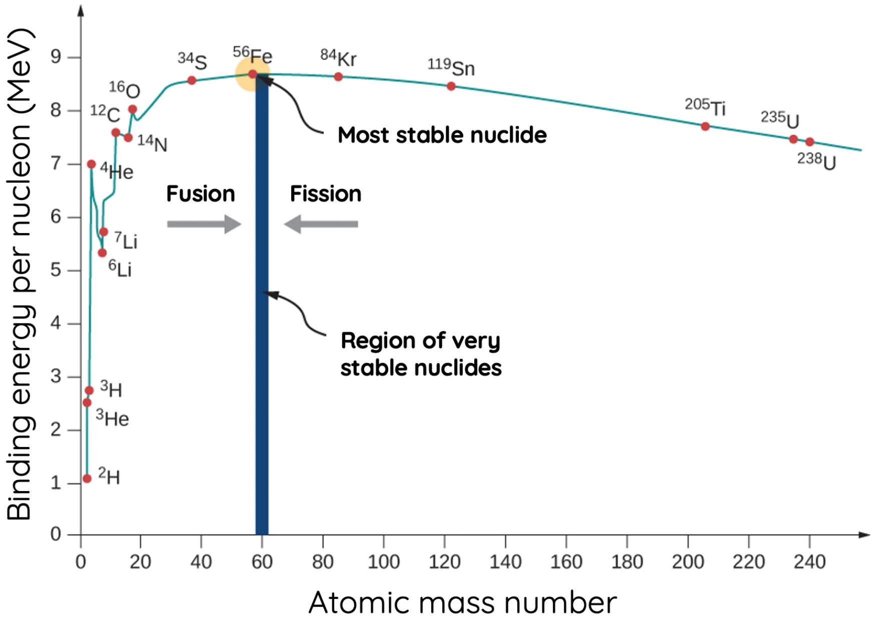

Figure 1.1: *Binding energy per nucleons, expressed in MeV as a function of atomic mass number nuclei, from Ref. [1].*

Another important parameter to consider is the cross-section of a given reaction $X_1 + X_2 \rightarrow X_3 + X_4$, denoted as σ_{X1X2} and usually expressed in barns (1 barn $= 10^{-28}\mathrm{m}^2$). It is defined as the ratio of the number of reacting nuclei X_1 per time unit to the number of impacting nuclei X_1 per time unit and surface unit. It depends solely on the relative velocity of nuclei X_1 and X_2. The rate coefficient $\langle \sigma(v) v \rangle$ is defined as the average of the cross-section σ_{X1X2} over the different velocities of all particles in an ensemble. As it can be seen in figure 1.2, the Deuterium-Tritium reaction is the most promising to be used in nuclear fusion power plants due to its higher rate coefficient $\langle \sigma v \rangle$ at relatively low energy. Note that the temperature are expressed in keV. In fact, in nuclear fusion, the term "temperature" commonly refers to the thermal energies (in K) multiplied by the Boltzmann constant $k_B = 8.61733326 \times 10^{-5}$ eV/K. In standard unit, they should be expressed in Joule. 1 eV correspond to approximately 11 600K.
The D-T reaction fuse together 2 hydrogen isotopes into a ^4He nucleus (also called α particles) and a free nuetron:

$$^{2}_{1}D \ + \ ^{3}_{1}T \implies \ ^{4}_{2}He \ (3.5 \ MeV) \ + \ ^{1}_{0}n \ (14.1 \ MeV) \tag{1.1}$$

A total energy of 17.6 MeV is released, split between the α particle and the neutron according to momentum conservation.

For the fusion reaction to happen, nuclei must be in close proximity, but their positive charges cause them to repel each other, so the charged particles have to overcome the Coulomb electrostatic barrier. In a classical world, the energy required is very high, but thanks to

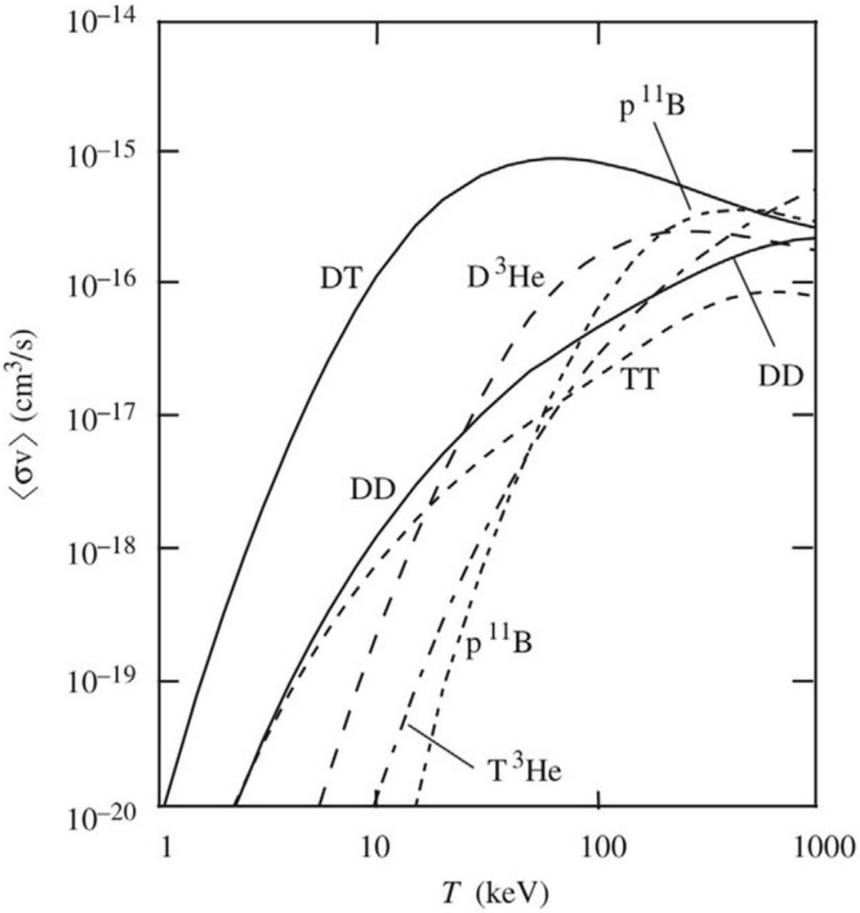

Figure 1.2: *Rate coefficient of easiest fusion reactions in function of temperature, expressed in keV. D-T reaction has a higher rate coefficient at low temperatures than other nuclear reactions. From [2].*

quantum tunnelling the temperatures required are of the orders of 10 $keV(\sim 10^8\ K)$.At this temperature the matter is in a plasma state, where atoms are ionized and electrons are detached from their nuclei, creating a quasi-neutral fluid that can conduct electricity and interact with electromagnetic fields.

The energy balance of the controlled thermonuclear fusion reaction is given by the total power generated by the fusion reaction P_F and the injected power P_H. To be a source of energy this difference should be positive. An important parameter that is used for measuring the performance of the fusion reaction is the amplification factor Q:

$$Q = \frac{P_F}{P_H} \tag{1.2}$$

When $Q = 1$ the fusion power equals to the injected power and it is called the break-even. While for $Q = 5$ the heating by α particles balances external heating. In addition, Q does not encompass the whole question of the energy efficiency of a fusion reactor. Since all additional losses due to the reactor components must be taken into account (i.e. the energy required by the pumps to circulate the coolant, ...), the value of Q necessary for "engineering breakeven" is in the order of 30 to 40.

The ignition regime corresponds to $Q \rightarrow \infty$, which is when the entire heating of the D-T fuel is provided by fusion born α particles. A fundamental quantity to achieve the ignition of a fusion reaction is the *Lawson criterion* or *Triple product*:

$$n \cdot T_i \cdot \tau_E \geq 3 \times 10^{21} \frac{keV\ s}{m^3} \tag{1.3}$$

Where n is the plasma density, T_i is the temperature of the reacting ions and τ_E is the confinement time of the plasma. τ_E is defined as the ratio between the overall thermal plasma energy W over the energy losses P_L: $\tau_E = W/P_L$ and is the physical quantity that estimates the confinement capability of a tokamak. After the plasma heating sources are switched off, the energy in the plasma volume decreases exponentially. τ_E is the time needed for the energy to decrease by a factor of e. The longer the confinement time, the better the confinement in the tokamak. τ_E should not be mistaken for the discharge duration, which can be much longer, lasting up to several minutes.

In stars, fusion occurs naturally due to the force of gravity, which counteracts the plasma's tendency to disperse and cool down. However, gravitational confinement is impossible on Earth and for very hot plasma ($T_i \sim 10\ keV$) alternative strategies must be employed. Two types of plasma confinement are mainly studied:

- Inertial confinement: that involves the use of high-power laser beams to concentrate extremely dense plasma ($n \sim 10^{31}\ m^{-3}$) for a brief confinement period ($\tau_E \sim 10^{-11}\ s$).
- Magnetic confinement: that aims to achieve energy confinement times of around one second ($\tau_E \sim 1\ s$) in low-density plasma ($n \sim 10^{20}\ m^{-3}$) using strong magnetic fields.

Despite inertial confinement fusion has achieved promising results in recent years [3], the concept of magnetic confinement thermonuclear fusion remains the most promising for a clean, carbon-free, reliable and economically feasible energy source.

This work focuses on magnetically confined plasma, which is the methodology studied at the IRFM. The following sections of this chapter provide further details on the physical principles underlying the research carried out during this thesis.

1.1.1 Magnetically confined plasma

As mentioned above, to achieve the ignition conditions, very high plasma temperatures ($T \sim 10keV \sim 10^8 K$) must be reached and no material currently available can withstand these temperatures. Hence, strong magnetic fields are used to confine the plasma and prevent it from coming into contact with the walls. That is possible because, as said before, plasma is a quasi-neutral mixture of charged particles so it is possible, thanks to the Lorentz force, to let charged particles follow the intense magnetic field lines by avoiding the plasma touching the wall's surface. In the lates decades, various magnetic configurations have been explored, with a focus on those that establish magnetic flux surfaces, effectively guiding magnetic field lines along bounded surfaces. Notable configurations are stellarators and tokamaks, both highly studied solutions. For example, the tokamak that aims to validate the feasibility of magnetically confined plasmas as a potential source of energy is the International Thermonuclear Experimental Reactor (ITER), which is under construction in Cadarache, in the south of France. This thesis focuses primarily on the study of tokamak plasmas in light of their importance in fusion research.

In tokamaks, the overall magnetic confinement results from the combination of two components: the toroidal magnetic field B_φ and the poloidal magnetic field B_θ. The former derives from a current flowing through external coils surrounding the toroidal chamber, while the latter is induced by the toroidal plasma current I_P inside the chamber. The poloidal magnetic field plays a key role in counteracting the pressure forces exerted by the confined plasma. To generate the plasma current, the transformer principle is used: the plasma acts as a secondary circuit while the magnetic flux in the central solenoid is modulated. The superposition of these two magnetic fields results in helical magnetic field lines. In addition to these components, current tokamaks, including ITER, incorporate additional coils with the task of adjusting the shape and position of the plasma. A representation of a tokamak device is shown in figure 1.3, in which the vertical coils are used to generate an additional vertical magnetic field component to control the plasma position and shape.

In the nuclear research center of Cadarache, the IRFM, the WEST or Tungsten (chemical symbol "**W**") **E**nvironment in **S**teady-state **T**okamak, (formerly Tore Supra) is currently in operation. The original name came from the words torus and superconductor, as Tore Supra was for a long time the only tokamak of this size (namely major radius of 2.5m and minor radius of 0.5m) with superconducting toroidal magnets, allowing the creation of a strong permanent toroidal magnetic field. However, ITER requires an essential component: the divertor, which receives most of the heat fluxes and particles from the central plasma during experiments. To test this component, a major upgrade to install tungsten walls and a divertor was done in Tore supra, leading to a modification to the magnetic configuration from its circular form to a distorted lens shape to obtain plasmas with characteristics similar to those of ITER. So the WEST tokamak enables researchers to conduct a relevant scientific program focusing on preparing experiments for ITER.

1.2 Basic introduction to tokamak plasma description

This section provides the physical fundamentals necessary to describe the behaviour of particles in tokamak plasma. For more comprehensive details on the following models and equations, refer to manuals on magnetized plasma physics and tokamak devices, such as [4], [5] and [6].

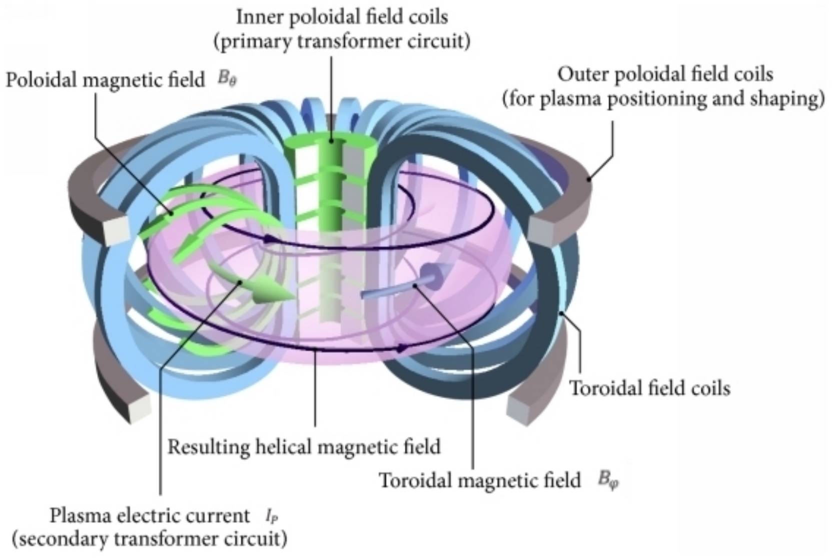

Figure 1.3: *Schematic view of a tokamak device. The inner torus represents the plasma, where the plasma current (I_P) generates the toroidal component of the magnetic field (B_θ). Surrounding the vacuum vessel are poloidal coils that generate the poloidal component of the magnetic field (B_φ). Additional coils produce the vertical component, which is essential for controlling the plasma's position. The resulting magnetic field lines, shown in their helical form, illustrate this complex magnetic configuration. Source: EUROfusion website*

1.2.1 Magnetic equilibrium in tokamaks

Various models can be used to represent plasma dynamics, each with a different level of description accuracy. As mentioned above, strong magnetic fields are used inside the tokakams to confine the plasma. For this reason, it is important to consider the interaction between charged particles that compose the plasma and electromagnetic fields. As presented earlier, these fields are a combination of external fields generated by the coils and those produced by the plasma itself.

This section introduces the concept of magnetic field equilibrium in a tokamak device and the coordinates used to define it. In a tokamak, the magnetic field is a continuous vector field, allowing the determination of tangent vectors known as magnetic field lines. For the charged particles in the plasma to be confined by these field lines, the lines must lie on closed surfaces, referred to as magnetic or flux surfaces. Due to the geometry of the tokamak, these magnetic surfaces are topologically toroidal, making toroidal coordinates $\mathbf{x} = (\rho, \theta, \varphi)$ convenient for describing this geometry. Here, ρ is the radial coordinates, while θ and φ represent the poloidal and toroidal (axisymmetric) angles, respectively. Two radii characterise a torus: the major radius R_0, the radius between the center of the axis of symmetry and the center of the poloidal section, and the minor radius a, the radius of the inner circle (the poloidal section). Two fundamental parameters to describe the tokamak are the ratio between these two radii called the *aspect ratio*:

$$A = R_0/a \tag{1.4}$$

and its inverse named the *inverse aspect ratio*

$$\epsilon = 1/A = a/R_0 \tag{1.5}$$

As a first approximation, a tokamak can be imagined as a straight cylinder (implying an infinite aspect ratio, $A \to \infty$) whose ends are joined together to form a torus, thereby achieving a finite aspect ratio. The aspect ratio is a critical parameter in tokamak design. Early tokamaks were characterized by large aspect ratios, meaning the plasma cross-section was relatively narrow compared to the overall size of the device. However, modern tokamak designs, such as the ITER, are moving towards configurations with lower aspect ratios. ITER, for instance, will have an aspect ratio of approximately 3, which helps to optimize the plasma confinement and stability while making the device more compact and efficient. Additionally, new configurations such as spherical tokamaks, which have an aspect ratio of less than 2, are being studied. These devices, which resemble a cored apple more than a traditional doughnut, offer potential advantages in terms of higher plasma pressure and better confinement properties, which could lead to more efficient and cost-effective fusion reactors.

Figure 1.4 illustrates a schematic representation of a circular cross-section toroidal geometry.

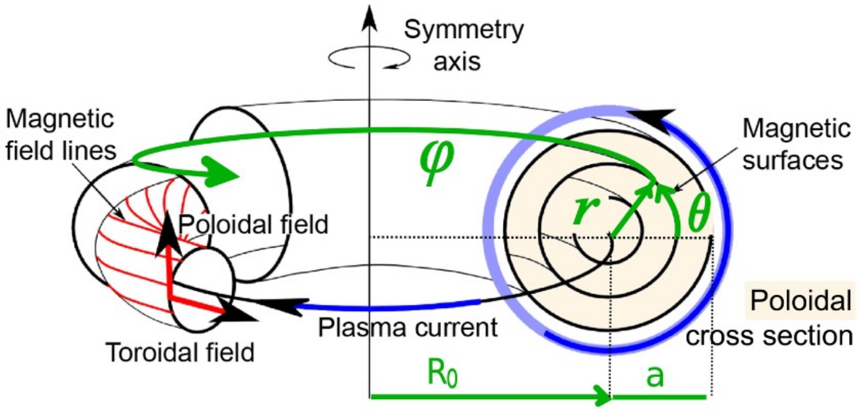

Figure 1.4: *Schematic view of the coordinate system for a tokamak device.*

In a constant magnetic field with straight field lines, charged particles are confined in the plane perpendicular to the magnetic field (transverse plane) but are free to move along the direction of the magnetic field (parallel direction). To achieve confinement in the parallel dimension, the field lines can be closed on themselves, forming circular loops. However, any inhomogeneity in the magnetic field, such as changes in its direction, results in a velocity drift perpendicular to both the magnetic field and its curvature or gradient. For horizontal circular field lines, this drift occurs vertically. To counteract the vertical drift caused by the circular field lines, a solution is to introduce a third periodic direction to the particle motion, confining their trajectory within a finite volume. This can be accomplished by generating a poloidal magnetic field, B_θ, which is aligned with the poloidal angle θ. In the presence of poloidal and toroidal components of the magnetic field, the magnetic field lines, which are always tangent to the magnetic field **B**, form helical paths winding around toroidal surfaces. These surfaces are known as magnetic field surfaces. The helicity of the magnetic field lines at each flux surface can be quantified by the safety factor q, which is defined as:

$$q(\rho_{tor}) = \frac{B_{eq} \cdot \nabla\varphi}{B_{eq} \cdot \nabla\theta} \tag{1.6}$$

where B_{eq} is the equilibrium magnetic field and ρ_{tor} is the normalized square root of the toroidal magnetic flux $\rho_{tor} = \sqrt{\Phi_{tor}/B_0}$ with Φ_{tor} is the toroidal magnetic flux. Essentially, the q parameter quantifies the ratio of toroidal to poloidal revolutions made by a magnetic field line, varying with each flux surface. If q is a rational number, the magnetic field line closes upon itself. However, if q is irrational, the magnetic field line spans the entire flux surface. Hence, it is possible to calculate the value of q for each flux surface, constructing the q-profile. Another relevant parameter related to the radial derivative of the safety factor is the magnetic shear:

$$\hat{s}(\rho_{tor}) = \frac{\rho_{tor}}{q}\frac{\mathrm{d}q}{\mathrm{d}\rho_{tor}} \tag{1.7}$$

All the relationships provided above remain valid regardless of the shape of the magnetic flux surfaces. However, for the sake of simplicity, Figure 1.4 illustrates a toroidal configuration of the magnetic field with circular and concentric flux surfaces.
This configuration with a circular poloidal section is the simplest, however different configurations in which magnetic topology of the flux surfaces exhibits substantial differences will be used in ITER, such as an axy-symmetrical X-point. Double null configurations are also being investigated. We will not analyse these configurations as only circular and concentric flux surfaces were utilised in this work.

1.2.2 Single particle motion

As discussed above, plasma is composed of charged particles that interact with the electromagnetic field present inside the tokamak. To describe the behavior of the plasma with the electromagnetic field we begin by discussing the interactions that a single particle has with the electromagnetic field. The simplest case that can be analyzed is that of a particle subjected only to a uniform magnetic field **B**, thus with electric field $\mathbf{E} = 0$. In this case, the particle will rotate around the magnetic field lines as shown in figure 1.5).
The Larmor radius r_L (Eq. 1.8), or gyroradius, is the radius of the rotation of the charged particle around the magnetic field line. It is influenced by the values of the charge of the particle q, the mass m, the magnitude of B and the component of the particle's velocity that is perpendicular to the magnetic field lines $v_\perp$.

$$r_L \ = \ \frac{v_\perp \, m}{|q|\mathbf{B}} \tag{1.8}$$

From relation 1.8 it can be seen that the larger is B the closer the particle is to the magnetic field line. In the case where a Cartesian coordinate system $S = (x,\ y,\ z)$ is considered and the magnetic field lines are exclusively aligned with the z-axis, the transverse plane's perpendicular velocity $v_\perp$ at time t for the particle located at position (x, y) is:

$$v_\perp = \sqrt{v_x^2 + v_y^2} \tag{1.9}$$

Each particle revolves around a central point known as the guiding center. The angle of rotation of the particle around this center is typically identified as Θ or gyroangle. The frequency at which the particle rotates around its guiding center is the *Larmor frequency* or *cyclotron frequency*:

$$\omega_{C0} = \frac{|q|\mathbf{B}}{m} = \frac{v_\perp}{r_L} \tag{1.10}$$

The direction in which the particle rotates around the guiding center is determined by the signs of its charge q (i.e. clockwise for negatively charged particles and anticlockwise for positively charged particles as it can be seen in fig. 1.5). Important not to confuse this q, which refers to the particle charge, with the *safety factor* q (Eq. 1.6) described above.

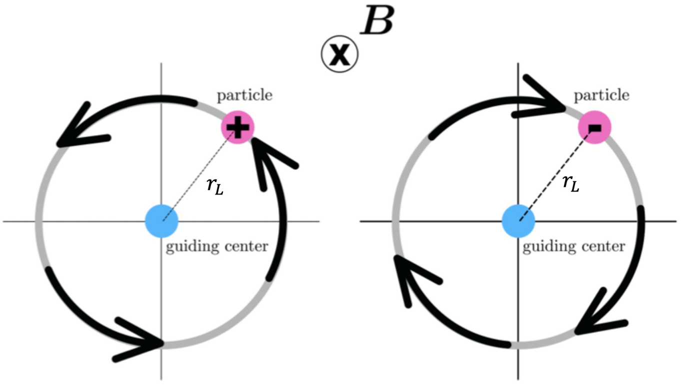

Figure 1.5: *Directions of rotation, in the transverse plane, of positively and negatively charged particles when magnetic field **B** are entering the page.*

The magnetic Lorentz force acts perpendicular to the magnetic field, so it does not impact the motion parallel to the field in the first approximation. In a uniform magnetic field and without any other forces present, a charged particle will rotate around the magnetic field lines based on the perpendicular component of its velocity. At the same time, it will move along the magnetic field lines according to its initial parallel velocity, resulting in a helical path (fig. 1.6).

If an electric field **E** is also taken into account, the particle will experience a drift (called **E** × **B** drift). If we have opposite charges they go in the same directions, but rotate in opposite directions (fig. 1.7a).
If the magnetic field **B** is inhomogeneous and the gradient of **B** is perpendicular to **B**

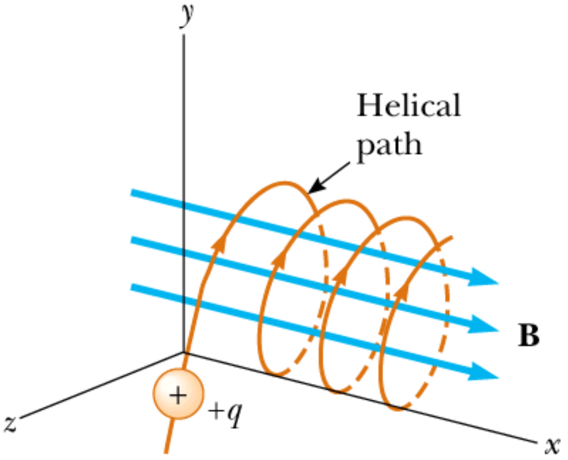

Figure 1.6: *Helical motion of a positively charged particle subject to a magnetic field **B** (from [7]).*

($\nabla B \perp \mathbf{B}$) there is the so-called grad-B drift. The gradient in $|\mathbf{B}|$ causes the Larmor radius to be larger at the bottom of the orbit than at the top. This leads to a drift, in opposite direction for ions and electrons, perpendicular to $\mathbf{B}$ and ∇B (fig 1.7b).
Due to the shape of the torus, the magnetic field is curvature, thus leading to the so-called curvature drift. The particles that moved along the magnetic field line felt a centrifugal force. That leads to the particles drifting out of the torus, no matter how one juggles the temperatures and magnetic field (fig. 1.7c).

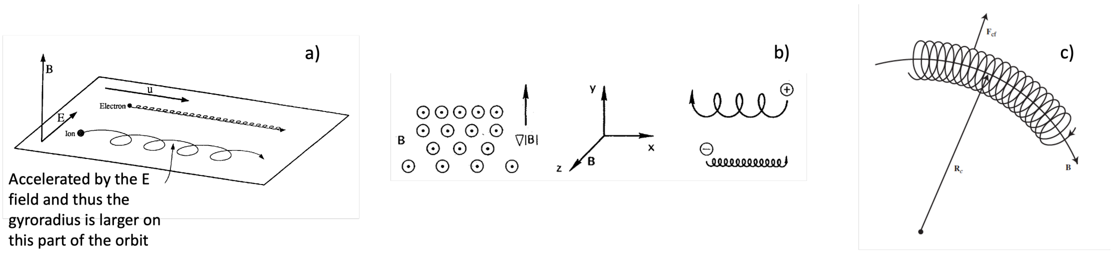

Figure 1.7: *Representatrion of the: $\boldsymbol{E} \times \boldsymbol{B}$ drift (a), ∇B drift (b) and curvature drift (c). From [8]*

1.2.3 Equation of motion of charged particles

Since plasma is composed of charged particles, it can interact with electromagnetic fields due to its nature. The most direct approach to describe plasma utilizes the equations of motion for each particle:

$$m\frac{d\mathbf{v}}{dt} = e(\mathbf{E} + \mathbf{v} \times \mathbf{B}) \tag{1.11}$$

where m is the mass of the particle, e is the charge of the electron and $\mathbf{v}$ the velocity of the particles. To take into account the collective effects of the particles on the electromagnetic fields, these equations are to be coupled with Maxwell equations in a medium:

$$\begin{aligned} \nabla \cdot \mathbf{D} &= \rho \\ \nabla \cdot \mathbf{B} &= 0 \\ \nabla \times \mathbf{E} &= -\frac{\partial \mathbf{B}}{\partial t} \\ \nabla \times \mathbf{H} &= \mathbf{j} + \frac{\partial \mathbf{D}}{\partial t} \\ \mathbf{D} &= \epsilon \mathbf{E} + \mathbf{P} \\ \mathbf{B} &= \mu \mathbf{B} + \mathbf{M} \end{aligned} \tag{1.12}$$

with **D** is the displacement electric field, **B** is the magnetic induction, ρ the charge density, **E** the electric field, **H** the magnetic field, **j** is the current density, ϵ the pemittivity, μ the permeability, **P** the polarization field and **M** the magnetization field. For simplicity, the magnetic field **H** will be intentionally confused with the magnetic induction **B** throughout the remainder of the thesis.

Solving these equations enables to determine the precise position $r(t)$ and velocity $v(t)$ of each particle in the system at any given time t. Although the equations involved are relatively straightforward, particularly when considering simplified cases, the number of vectorial equations and particles must be equal. Since the density of the plasma can be as high as 10^{20} $particles/m^3$, this poses a great problem such as computational complexity, difficulties in analytical resolution and numerical stability problems, and therefore different approaches are used that tend to reduce the number of independent variables of the system.

1.2.4 Kinetic description

One approach to study plasmas is through statistical mechanics: it implies the derivation of kinetic equations from the equations of motion of individual particles, typically in Hamiltonian form. The distribution function, denoted as $F(\mathbf{x},\ \mathbf{v},\ t)$, is a commonly used solution to describe the plasma, representing the expected number of particles with position $[r\ +\ dr]$ and velocity $[\mathbf{v}\ +\ d\mathbf{v}]$ at a given time. While kinetic equations can provide more interpretable results than other methods, they can still be challenging for computers to handle due to the seven variables involved in $F(\mathbf{x},\ \mathbf{v},\ t)$, 3 for the position $\mathbf{x}$, 3 for the velocity $\mathbf{v}$ plus the time. However, distribution functions can be used to obtain useful quantities such as plasma temperature and density. In the absence of particle interactions, such as collisions, the Liouville theorem states that the distribution function F remains constant along the paths traced by the total phase space. In other words, as a particle moves along its path in phase space, the value of F does not change. As a result, the density of the total phase space remains conserved during the time interval Δt. This means that if a fixed volume in phase space is considered, the total number of particles within this volume remains constant over time if there are no collisions. Therefore, in the absence of collisions, the probability distribution function for the particle trajectory across the entirety of the phase space, denoted as $P = (\mathbf{x},\ \mathbf{v},\ t)$, remains constant. This means that the probability of finding a particle at a given position $\mathbf{x}$ with a given velocity $\mathbf{v}$ at time t does not change as the particle moves. This relation is expressed through the *Vlasov* or *kinetic* equation:

$$\frac{dF}{dP} = \frac{\partial F}{\partial t} + \mathbf{v} \cdot \nabla F + \frac{eZ}{m}(\mathbf{E} + \mathbf{v} \times \mathbf{B}) \cdot \nabla_{\mathbf{v}} F = 0 \tag{1.13}$$

The time derivative $\partial F/\partial t$ represents the time rate of change of the distribution function F at a fixed point in phase space. It accounts for how the distribution function evolves over time. The term $\mathbf{v} \cdot \nabla F$ is the advection in real space and it represents the spatial transport of particles, that is the movement of particles through physical space due to their velocities. Here, ∇F is the spatial gradient of the distribution function. This term describes how particles move through space. The term $\frac{eZ}{m}(\mathbf{E} + \mathbf{v} \times \mathbf{B}) \cdot \nabla_{\mathbf{v}} F$ is the advection in velocity space and it describes the influence of external electromagnetic fields on the particle distribution function. $\mathbf{v} \times \mathbf{B}$ gives the magnetic force on the particle and $\mathbf{E} + \mathbf{v} \times \mathbf{B}$ is the Lorentz force, which is the total electromagnetic force acting on a charged particle. $\nabla_{\mathbf{v}} F$ is the gradient of the distribution function with respect to velocity. This term describes how the distribution function changes in velocity space due to the electromagnetic force. In equation 1.13, only the plasma's system collective effects, produced by the particle ensemble, are considered.

In the plasma inside a tokamak, the collision frequency is negligible compared to the collective effects, however, collisions play an important role in transport phenomena, changing the particle phase space and leading to possible instabilities. The Vlasov equation to which a collisional term is added is called the *Fokker -Plank equation*:

$$\frac{\partial F}{\partial t} + \mathbf{v} \cdot \nabla F + \frac{eZ}{m}(\mathbf{E} + \mathbf{v} \times \mathbf{B}) \cdot \nabla_{\mathbf{v}} F = \left(\frac{\partial F}{\partial t}\right)_c \tag{1.14}$$

where the term $(\partial F/\partial t)_c$ is added to take into account collisions, defining a collective behaviour, since it is considered the whole distribution function F. A statistically self-consistent representation of the plasma system, encompassing both particle and field dynamics, is obtained by combining the Maxwell equations 1.12 and the Fokker-Plank equation 1.14.

1.2.5 Overview of wave-particle interaction

The interaction between waves and particles can excite kinetic instabilities in a magnetized plasma. In addition, some external heating systems use wave-particle interactions to deliberately deposit energy on the ions (Ion Cyclotron Resonance Heating, or ICRH), electrons (Electron Cyclotron Resonance Heating, or ECRH and Lower Hybrid Current Drive, or LHCD). This is a fundamental aspect that will be described later in this thesis.

A kinetic approach is necessary to describe this interaction since the movement of charged particles in magnetized plasma results in the generation of waves, which can then interact with the particles under specific resonant conditions in the velocity phase space. The exact solution of the Vlasov equation (1.13) helps describing the wave-particle interaction phenomena. To simplify the solution, it is possible to use an approach called δf-splitting, which consists of separating the static background of the distribuction function F_0 from its perturbed part δf, thus obtaining the relation $F = F_0 + f$ (where $\langle f \rangle = 0$ and $f \ll F_0$). Neglecting the magnetic field ($\mathbf{B} = 0$), writing the electric field $\mathbf{E} = -\partial\phi/\partial\mathbf{x}$ (were ϕ is the electrostatic potential) and using the δf-splitting, the Vlasov equation is linearized:

$$\frac{\partial f}{\partial t}\,\mathbf{v}\cdot\left(\frac{\partial F_0}{\partial \mathbf{x}} + \frac{\partial f}{\partial \mathbf{x}}\right) + \frac{eZ}{m}\cdot\frac{\partial \phi}{\partial \mathbf{x}}\cdot\frac{\partial F_0}{\partial \mathbf{v}} = 0 \tag{1.15}$$

Once linearizing the Vlasov equation, it becomes feasible to find the eigenvectors associated with the perturbed distribution function and the electrostatic potential ϕ. These eigenvectors manifest as plane waves characterized by the expression $\hat{A}e^{i(\mathbf{k}\cdot\mathbf{x}-\omega t)}$, where $\mathbf{k}$ denotes the wavevector and ω represents the frequency. By replacing the eigenvector in 1.15 it is possible to obtain the exact solution that describes the fluctuation of the particle distribution function:

$$\hat{f} = -\frac{\frac{eZ}{m}\hat{\phi}\mathbf{k}\cdot\frac{\partial F_0}{\partial \mathbf{v}} + \mathbf{v}\cdot\frac{\partial F_0}{\partial \mathbf{x}}}{\omega - \mathbf{k}\cdot\mathbf{v}} \tag{1.16}$$

By coupling this relationship with the Poisson equation, we obtain a relationship through which the interaction between particle dynamics and electromagnetic field fluctuations is described:

$$\nabla^2\hat{\phi} = -eZ\int \hat{f}\,d\mathbf{v}\ (+\text{ non-resonant terms}) \tag{1.17}$$

That relation is written only for one species in the system, which is consistent with the assumption of non-overlapping dynamics between different species, such as electrons and ions. The essence of wave-particle interaction is encapsulated in the denominator of relation 1.16: in the terms $\omega - \mathbf{k}\cdot\mathbf{v}$, which establish a connection between the wave parameters ω and $\mathbf{k}$ and the particle dynamics (expressed by particle velocity $\mathbf{v}$). It is crucial to emphasize that for effective wave-particle interaction, the condition $\omega \sim \mathbf{k}\cdot\mathbf{v}$ needs to be satisfied, rather than an exact equality of $\omega = \mathbf{k}\cdot\mathbf{v}$. This is because when $\omega = \mathbf{k}\cdot\mathbf{v}$ precisely, the wave moves at the same velocity as the particles, so it cannot give or receive energy to the particles themselves.

In the numerator of relationship 1.16, are present two key parameters that determined the wave-particle resonant condition: the gradient in velocity phase space $\partial F_0/\partial\mathbf{v}$ and the spatial gradient $\partial F_0/\partial\mathbf{x}$, these gradients dictate the direction of net energy transfer between waves and particles. Taking $\partial_x F_0$ as an example, it reflects the radial temperature gradient of the particle distribution, typically negative from the core to the plasma edge. In a localized plasma region near the flux surface of interaction, the higher-temperature particles outnumber their lower-temperature counterparts due to the negative slope of the distribution ($\partial_x F_0 < 0$). Consequently, there is a positive net energy transfer from particles to waves, causing possible instability. Conversely, a positive slope of the radial distribution ($\partial_x F_0 > 0$) results in energy transfer from waves to particles, thus the waves are damped. Shifting the focus to $\partial_v F_0$, the scenario reverses: a positive slope in velocity space ($\partial_v F_0 > 0$)leads to more particles giving energy to the wave than receiving it, driving instability through the positive gradient of the equilibrium distribution in the velocity space.

1.2.6 Gyrokinetic theory

As previously mentioned, the statistical kinetic depiction of particle trajectories in a magnetized plasma demands significant computational resources. Despite these challenges, it is imperative to consider resonant mechanisms occurring in the velocity space to capture essential physics when examining the tokamak plasma core. A well-established theoretical framework to reduce the 6-dimensional system of equations inherent in the kinetic approach to more manageable 5 dimensions is the gyrokinetic approach. In this thesis, we will not go through the detailed mathematical steps leading to this reduction(for further details see [9] and [10]). Instead, our emphasis will be on highlighting the advantages gained by employing this approach.
The gyrokinetic approximation ensures that any characteristic frequency retained is indeed much lower than the cyclotron frequency (Eq. 1.10) and the spatial scales associated with the described phenomena are much larger than the Larmor radius (Eq. 1.8). In this framework, transitioning from a 6-dimensional representation to a 5-dimensional one involves a shift from particle position to the guiding-center set of coordinates (figure 1.8). The coordinates of the guiding centre ($\mathbf{x}_g$))(the position of the centre of the cyclotronic trajectory, visible in figure 1.5) are used to describe the motion of the particles. The equations of motion for the guiding centre are derived by applying the cyclotronic average (a time average of the rapid cyclotronic motion) to the equations governing the motion. As a result, the distribution function is no longer dependent on the full particle phase space ($\mathbf{x},\ \mathbf{v},\ t$), but is now denoted as $\bar{F}(\mathbf{X}, v_\parallel, \mu, t)$, where $\bar{F}$ indicates the gyro averaged distribution function, $\mathbf{X}$ is the guiding center position in space, $v_\parallel$ is the parallel velocity along the magnetic field line and μ is the magnetic moment of the particle:

$$\mu = \frac{mv_\perp^2}{2B} \tag{1.18}$$

where $v_\perp$ is the velocity of the particle in its cyclotron motion. The gyro-center reduction hinges on the conservation of the magnetic moment μ of the cyclotron loop, which is linked to its radius. The preservation of the magnetic moment enables a further simplification of the model. This is because the kinetic dynamics for different values of μ become independent, contributing to a more streamlined and manageable representation. In terms of simulation cost, this last point is convenient because μ plays the role of a parameter. This means that the problem to treat is not a true 5D problem but rather a 4D problem parametrized by μ. Note that μ loses its invariance property in the presence of collisions. Such a numerical drawback can be overcome by considering reduced collision operators acting in the $v_\parallel$ space only, while still recovering the results of the neoclassical theory [11].

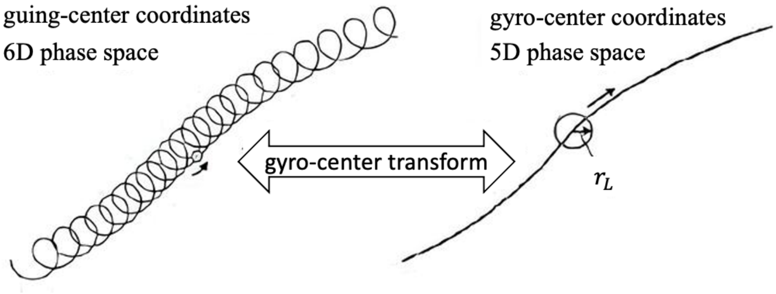

Figure 1.8: *Example of the gyro-center transform of a particle trajectory used in the gyrokinetic description (from [12]).*

1.3 Instabilities driven by fast ions in tokamaks

A significant factor to be taken into account to successfully confine the plasma and thus use nuclear fusion as an alternative energy source is the establishment of instabilities, which can cause what is known as turbulent transport in a non-linear regime. This turbulent transport surpasses neoclassical (collisional) transport [13] by more than an order of magnitude, significantly limiting the confinement performance of current fusion devices. However, instabilities are nearly inevitable in a magnetized fusion plasma, given its out-of-equilibrium nature. Even a slight perturbation in the electromagnetic field can result in fluctuations in the particle distribution function, as demonstrated in relation 1.16. Specifically, when steep gradients exist in both spatial $\mathbf{x}$ and velocity $\mathbf{v}$ phase spaces of the particle distribution function, the initial perturbation can grow unstable, the gradients $\partial_v F_0$ and $\partial_x F_0$ act as reservoirs of free energy for these growing instabilities [14]. Although instabilities in a magnetized plasma can manifest in diverse forms, the focus in the remainder of this thesis will primarily be on high-frequency fast-ion-driven instabilities. These macroscopic instabilities have a broad-reaching impact, affecting a substantial portion of the entire plasma volume.

While the plasma in thermodynamic equilibrium is accurately characterized by the isotropic Maxwellian distribution function, decreasing at higher particle energies, the impact of fast ions (or energetic ions) on plasma stability is anticipated to be marginal. However, in both current and future fusion devices, the presence of fast ions, possessing much higher energy than the bulk particles, is unavoidable. Notably, alpha particles with an energy of 3.5 MeV are inherent products of the total fusion reaction and play a crucial role in sustaining the overall process by transferring their energy to the thermal part of the plasma through Coulomb collisional interactions. Additionally, externally generated fast ions serve the purpose of heating the bulk particles. The main external fast-ion sources are the Ion Cyclotron Resonance Heating (ICRH) and the Neutral Beam Injection (NBI). Both fusion-born alpha particles and externally generated fast ions alter the tail of the ion distribution function. In the case where the distribution function is non-monotonic, the primary driver of instabilities is the bump generated in the velocity phase space. A schematic representation of such a bump is illustrated in Figure 1.9.

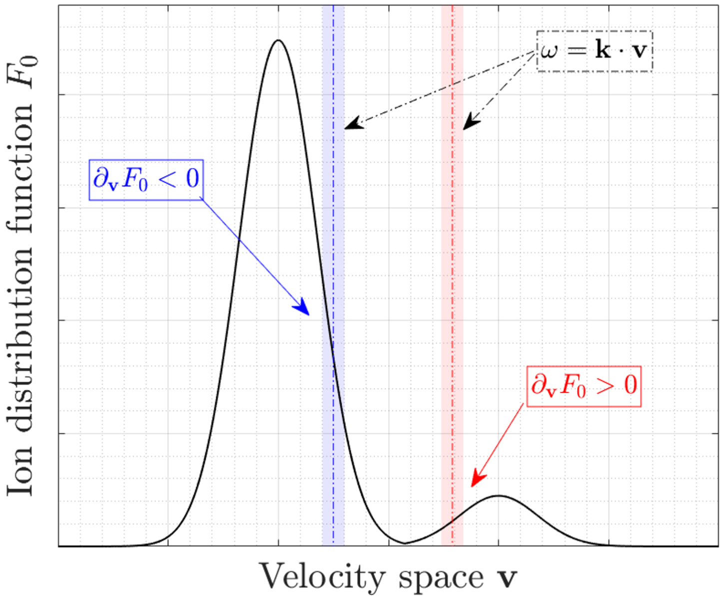

Figure 1.9: *Illustration of a non-monotonic ion distribution function in velocity space, with indications of the sign of the gradient in this space. This emphasises the mechanism of excitation of instabilities in plasmas through wave-particle resonance (from [14]).*

As depicted in Relation 1.16 and discussed in section 1.2.5, the contribution to the destabilization of fast-ion-driven instabilities can arise from spatial gradients of the equilibrium distribution, specifically radial gradients, as well as gradients in the velocity phase space. Particularly, the wave-particle interaction is significantly influenced by the terms $\partial_x F_0$ and $\partial_v F_0$, which dictate the direction of energy transfer: when $\partial_x F_0 < 0$ and $\partial_v F_0 > 0$, the energy transfer is from the particle to the wave and it can be associated to excitation mechanism. Conversely, if $\partial_x F_0 > 0$ and $\partial_v F_0 < 0$, the energy transfer occurs from the wave to the particle, leading to damping phenomena. Hence, the presence of steep, monotonically decreasing radial gradients and the generation of a bump in the ion distribution function can initiate fast-ion-driven instabilities independently. These instabilities, in turn, can have adverse effects on plasma stability. Fast ions, while transferring their energy to the wave, are consequently transported from the hotter central region of the plasma to the cooler edge, where lower temperatures prevail. Only one type of instability is presented in this article; for a comprehensive overview of all these instabilities refer to [15], [16], [17] and [18]

1.3.1 Shear Alfvén Waves

The instability examined is the Shear Alfvén Waves (SAW). Alfvén waves are transverse low-frequency electromagnetic waves, in particular, they are waves propagating in the parallel direction with respect to the magnetic field lines due to perpendicular perturbation of the equilibrium magnetic field **B** [19] that propagates with Alfvén velocity $v_A = B_0/(\sqrt{\mu_0 \rho_d})$, with ρ_d the plasma mass density. This velocity falls within the range of motion dynamics for fast ions in tokamak plasmas. Consequently, interactions between the waves and particles can take place. The subsequent section provides a fundamental overview of the physical framework surrounding SAW excitation, commencing with an introduction to Alfvén waves.

Alfvén waves always exist in a conducting fluid, such as plasma, immersed in an external magnetic field, regardless of the system's geometry. When considering tokamak plasmas, the bending of magnetic field lines and the introduction of magnetic shear (Eq. 1.7) become relevant factors, as viewed in section 1.2.1. Considering this, the velocity of Alfvén waves varies radially within the plasma region. Due to this radial dependency, the Alfvén waves in tokamaks are specifically referred to as Shear Alfvén Waves.
When the wave frequency ω is small compared to the ion cyclotron frequency ω_{C0} (Eq. 1.10) and when kinetic effects are unimportant [17], the dispersion relation in a uniform field for the Shear Alfvén waves, derived under the incompressible ideal MHD limit (i.e., for $E_\parallel = 0$) and in a cylindrical configuration (namely with great value of aspect ratio A (Eq. 1.4) or inverse aspect ratio $\epsilon \ll 1$ (Eq. 1.5)), is expressed as:

$$\omega_{SAW}^2 = k_\parallel^2(r) \cdot v_A(r)^2 \tag{1.19}$$

where $k_\parallel = (m - nq)/(qR_0)$ is the parallel wave vector of the magnetic field and q is the safety factor (Eq. 1.6) that usually is a function of radius. This implies that the dispersion relation 1.19 is a function of radius in a sheared magnetic field [17]. Collectively, these solutions constitute the Alfvén continuum for various values of $k_\parallel$. An illustration of the Alfvén continua is presented in Figure 1.10, considering a constant toroidal number n and successive poloidal mode numbers m.

However, in a realistic tokamak, going from a cylindrical to a toroidal configuration, the value of the inverse aspect ratio (Eq. 1.5) is not close to 0 and so the aspect ratio (Eq. 1.4) is not great anymore (i.e. in ITER the aspect ratio $A = 3$). This leads to a coupling between neighbouring poloidal harmonics with mode numbers m and $m + 1$. Consequently, the dispersion relation for the two coupled branches can be expressed as [20]:

$$\omega_{TAE}^2 = \frac{k_{\parallel,m}^2 v_A^2 + k_{\parallel,m+1}^2 v_A^2 \pm \sqrt{(k_{\parallel,m}^2 v_A^2 - k_{\parallel,m+1}^2 v_A^2)^2 + 4\epsilon^2 r^2 k_{\parallel,m}^2 v_A^2 k_{\parallel,m+1}^2 v_A^2}}{2(1-\epsilon^2 r^2)^2} \tag{1.20}$$

where the two branches can be referred as ω_{TAE}^+ and ω_{TAE}^-. As illustrated in figure 1.11 this coupling leads to a gap in the continuum spectrum in the overlapping point, where the two branches open a gap. As a result, Alfvén waves remain undamped by phase mixing effects within this gap, facilitating their unstable growth. The undamped eigenfunctions residing in this gap, brought about by the toroidicity of the plasma system, are termed Toroidal Alfvén Eigenmodes (TAEs).

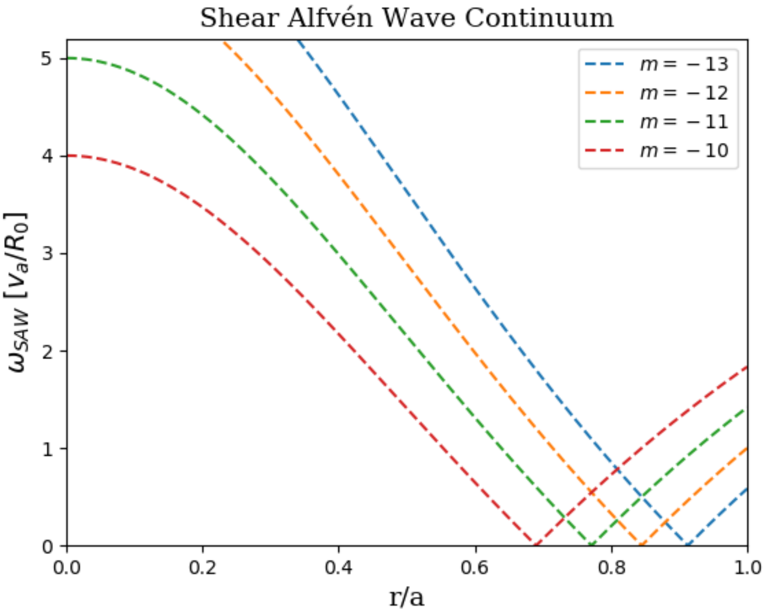

Figure 1.10: *Shear Alfvén Waves (SAW) continuum in cylindrical configuration produced by plotting relation 1.19 as a function of normalised radial direction r/a for $n = 2$ and $m = [-13, -10]$.*

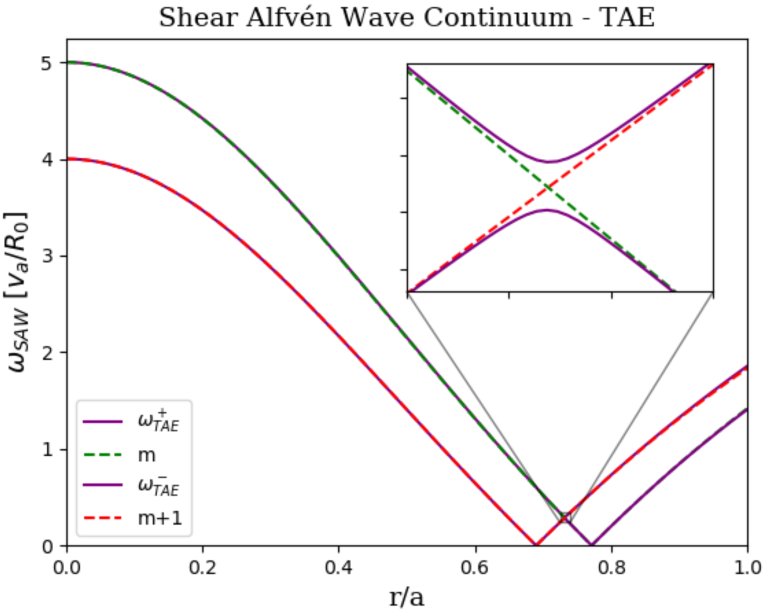

Figure 1.11: *Shear Alfvén waves spectra (solid curves) in toroidal configuration produced by plotting relation 1.20 as a function of normalised radial direction r/a for $n = 2$ and $m = -11$ and $m+1 = -10$. The red and blue dashed curves represent the continua in cylindrical geometry*

Frequency gaps are important because radially extended and the mode are not subject to continuum damping. So undamped eigenfunctions can exist in these gaps [17]. This toroidicity-induced gap is centred at:

$$\omega = \frac{v_A}{4\pi q R} \tag{1.21}$$

that varies with the radius, since v_a/q varies with the radius, moving to lower frequencies with increasing radius. The width of the gap depends on the variations in the field strength since the gap is proportional to $\Delta B = B_0 - B(r)$. That means that the width of the gap increases with radius because ΔB increases as r/R increases [17].

There are additional types of instability related to Alfvén waves in tokamaks:

- **Ellipticity-induced Alfvén Eigenmodes (EAEs)**: These instabilities occur due to the ellipticity of the plasma, meaning the deviation from cylindrical symmetry of the plasma within the tokamak.
- **Beta-induced Alfvén Eigenmodes (BAEs)**: caused by the effect of plasma pressure (beta) on Alfvén waves. Beta represents the ratio of plasma pressure to magnetic pressure.
- **Alfvén Cascades (ACs)**: These instabilities are characterized by a cascading spectral structure and are observed during the current ramp-up phase in tokamaks.
- **Kinetic Alfvén Waves (KAWs)**: These waves occur when kinetic effects, such as the non-thermal distribution of particles, become significant.
- **Global Alfvén Eigenmodes (GAEs)**: GAEs are global instabilities that extend over a large part of the plasma and are influenced by the overall geometry of the tokamak.
- **Compressional Alfvén Eigenmodes (CAEs)**: These instabilities involve compressions of the magnetic field and field lines, in addition to the normal transverse oscillations of Alfvén waves.

All these types of Alfvén instabilities can significantly affect the confinement and stability of the plasma in tokamaks, making their study crucial for the advancement of controlled nuclear fusion. However, we will not go into these in detail as this work focuses solely on the study of TAEs. For a more in-depth analysis of the phenomenology of Alfvén eigenmodes refer to [21] and [22].

1.3.2 Alfvén eigenmode and fast ions

In the previous paragraphs, it has been observed that Alfvén Eigenmodes (AEs), can persist undamped within an open gap in the Alfvén continuum. These modes can interact with the motion of fast ions, resulting in the excitation of instabilities. This happens when the fast ion contribution exceeds a specific threshold, usually when the fast ion pressure matches the thermal pressure, and the phase mixing effects fail to damp the propagating wave sufficiently. As a result, the wave can become unstable and absorb energy from the fast particles. The frequencies of the AEs are determined by the gaps in the continuum, which in turn are influenced by the characteristics of the plasma background. Consequently, the various AEs can only span a limited range of frequencies, wherein resonant conditions between the undamped eigenmodes and the characteristics of fast-ion motion prevail.

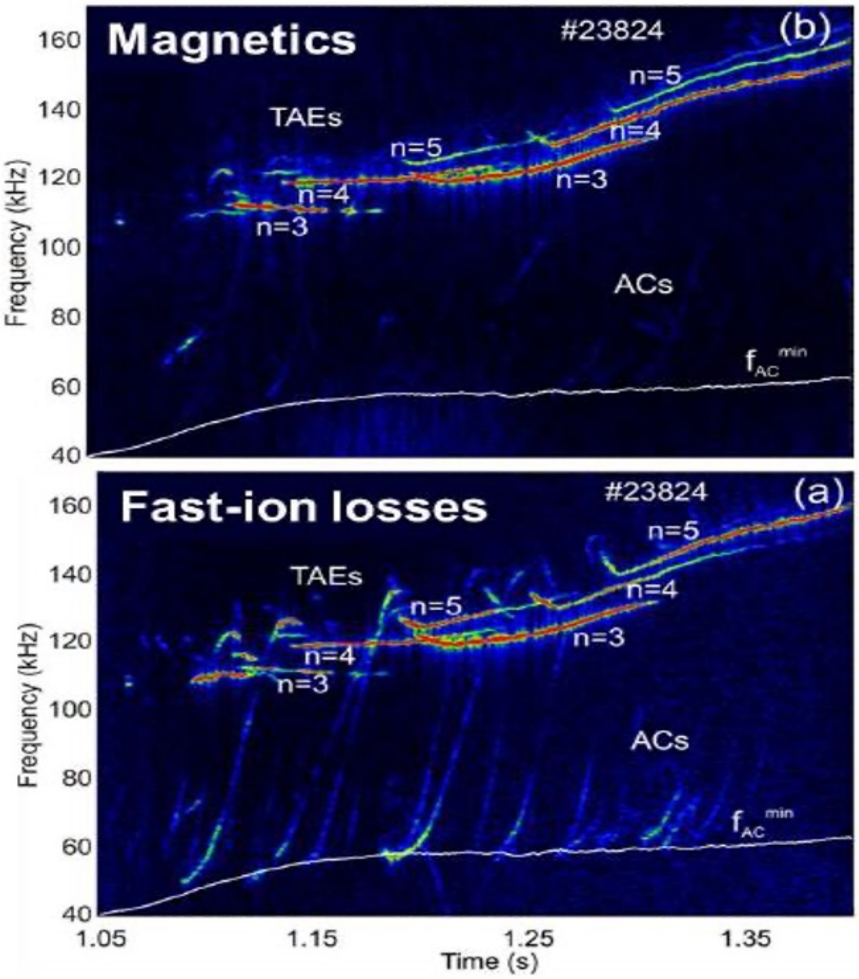

Figure 1.12: *Fourier spectrogram of an in-vessel magnetic pickup coil (b) and from probes measuring the fast-ion losses (a) taken in the tokamak ASDEX upgrade. (from [23]). It is possible to see the correlation between the instabilities due to the TAE and the loss of fast ion.*

The correlation between the continuum and fast ion losses is an experimentally observed phenomenon [23]. Figure 1.12b and 1.12a show respectively the Fourier spectrogram for a magnetic fluctuation signal measured by an in-vessel magnetic pick-up coil and for a soft x-ray (SXR) signal that measure the loss of fast ion. Several coherent MHD fluctuations are visible around 110 kHz up to 170 kHz. They correspond to TAEs with different toroidal mode numbers n's ($n = 3, 4, 5$). As can be seen, there is a clear correlation between the gaps in the continuum and the loss of fast ions. This loss of fast ion leads to a loss of performance, as shown in section 1.2.5.

1.4 Thesis outline

This chapter introduced the basics of controlled thermonuclear fusion, the basic principles of magnetic confinement of plasmas in tokamaks, and various models to describe its behaviour. Finally, a brief introduction to instabilities in tokamaks has been made, focusing on the instabilities driven by fast ions and in particular the Alfvén Eigenmodes, as they are the main focus of this thesis.

Chapter 2 will provide a presentation and brief introduction to the numerical code (GYSELA) I used during this work, in particular the focus will be on the underlying gyrokinetic model and how the Poisson equation is solved, a useful step in understanding the implementations in the code that I made later on. Chapter 3 will present the results of numerical simulations we performed to understand the Alfvén eigenmode phenomenon within the GYSELA code. This thesis aims to understand how the destabilisation mechanism of TAEs works within GYSELA, so Chapter 4 will discuss and expose the modifications I made within the code to pursue this goal. Finally, the results of these implementations will be presented.

Chapter 2

GYSELA code

As explained in Chapter 1.2, plasmas within the tokamak core exhibit low collisionality, so fluid models show limitations in describing them appropriately, preferring kinetic descriptions. The kinetic formalism is necessary to take the wave-particle interaction into account. In this approximation, the evolution of the 6-dimensional distribution function is solved for each species via the Vlasov or Fokker-Plank equation (eq. 1.14) by coupling it to the self-consistent equations for electromagnetic fields (the well-known Maxwell equations 1.12). Since turbulent fluctuations develop at much lower frequencies compared to the high-frequency cyclotron motion, it is possible to reduce the phase space by eliminating gyroscopic motion and other high-frequency dynamics (such as ideal MHD modes, electrostatic high-frequency waves and fast microscopic effect), thus moving from a 6D to a 5D problem. This model, called gyrokinetic, allows the distribution function to evolve into a 5-dimensional phase space, generated by four slow variables and an adiabatic invariant (μ, eq. 1.18) Given the complexity of this phenomenon, gyrokinetic codes developed for this purpose rely heavily on massively parallel supercomputers and state-of-the-art high-performance computing (HPC) [24].

For the study of TAE, it has been used the Gyrokinetic code GYSELA, developed at IRFM with the aim to analyse in detail what happens inside the plasma core. In this chapter, a brief description of GYSELA will be given. This part is mainly based on [24] and [25].

2.1 GYSELA characteristics

GYSELA is a semi-Lagrangian non-linear global flux-driven full-f electrostatic gyro-kinetic code for tokamak turbulence simulations (GYSELA stands for GYrokinetik SEmi-LAgrangian code).

- **Backward semi-Lagrangian**:
  the semi-Lagrangian method combines elements of both the Lagrangian and Eulerian approaches to provide an accurate description of phase space, particularly in regions of low density, while also enhancing numerical stability. This method capitalizes on the precision offered by solving convection (or advection) hyperbolic Partial Differential

Equations (PDEs) using their characteristics, along which the distribution function remains constant. Key features of the semi-Lagrangian method include:

  - conservation of a fixed phase-space mesh grid over time (Eulerian method),
  - integration of the Vlasov equation along trajectories (Lagrangian method), exploiting the invariance of the distribution function along these trajectories. When considering each arrival phase space position $\left(\mathbf{X}, v_{\parallel}, \mu\right)$, the scheme calculates the particle's trajectory in reverse, determining its position at an earlier time. The distribution function at the arrival time is then derived by interpolating the earlier distribution at the particle's initial position.

  This allows to take advantage of both methods, to achieve limited numerical dissipation with limited numerical noise.

- **Non-linear**:
  the trajectories of the particles encompass the entire E × B drift without any separation between equilibrium flow and perturbations.
- **Global**:
  the code simulates the entire plasma core, from the central region to the boundary.
- **Flux-driven**:
  to better mimic the experimental setup, where all the quantities evolve on equal footing, the dynamics are driven by a heat source near the core, allowing them to be transported, and any excess is removed at the edge. Consequently, the properties adapt to the transport and they are not fixed, evolving self-consistetnly.
- **Full-*f***:
  the code simulates the complete distribution function.
- **Electromagnetic**:
  the code calculates both the evolution of the electrostatic potential Φ and electromagnetic potential $\mathbf{A}$, in particular, the magnetic fluctuations are carried by the parallel component of the magnetic vector potential $A_{\parallel} = \mathbf{b} \cdot \delta\mathbf{A}$, where $\mathbf{b}$ is the vector along the magnetic field line at the guiding-center position.

Given the accurate and complete description of the phenomena occurring within the plasma core, the simulations performed with GYSELA cost 2 million CPU hours for approximately 1 millisecond in real-time [25]. The code is developed in Fortran 90, with some input/output routine written in C (47k lines of Fortran 90 and 2.3 lines of C code) [24].

2.2 Brief overview of full-*f* gyrokinetic Vlasov equation in GYSELA

In those paragraphs, an overview of the equations that are used in GYSELA is presented. It must be taken into account that the electromagnetic part of the code was developed quite

recently thanks to Gillot's work [25] and is still being studied by Bigue's work [26] in his ongoing PhD thesis.
In GYSELA the magnetic topology is fixed and consists of concentrical toroidal magnetic surfaces with circular poloidal cross-sections. the current is decoupled from the field and the magnetic field is assumed to satisfy the Ampère equation, but not the force balance equation. Consider the gyro-center coordinate system $(\mathbf{x}_G, v_{G\|}, \mu_s)$ where $\mathbf{x}_G$ represent the 3D space coordinates, (i.e. the set of coordinates (x^1, x^2, x^3) is equal to (r, θ, φ)), $v_{G\|}$ the velocity parallel to the magnetic field line and μ_s the magnetic moment $\mu_s = m_s v_{G\perp}^2/(2B)$, here m_s the mass of the species s taken into account. These are the same variables described in paragraph 1.2.6 with a notation changed to be consistent with the one used in GYSELA equation of [24]. Denote with F_s the particle distribution function and with $\bar{F}_s$ the one associated with the guiding-center. GYSELA models for each species s the time evolution of the guiding-center distribution function $\bar{F}_s$, without separating the equilibrium and perturbation and this is the *full-f* treatment. GYSELA solves a set of gyrokinetic equations:

i) one collisional gyrokinetic equation that describes the non-linear time evolution of $\bar{F}_s$ for each ion species in the 4D phase space parametrized by the adiabatic invariant μ:

$$B^*_{\|s} \frac{\partial \bar{F}_s}{\partial t} + \nabla \cdot \left(B^*_{\|s} \frac{\mathrm{d}\mathbf{x}_G}{\mathrm{d}t} \bar{F}_s \right) + \frac{\partial}{\partial v_{G\|}} \left(B^*_{\|s} \frac{\mathrm{d}v_{G\|}}{\mathrm{d}t} \bar{F}_s \right) = \mathcal{R}hs \left(\bar{F}_s \right) \tag{2.1}$$

that equation is known as the *Boltzmann equation*, where $B^*_{\|s} = \mathbf{B}^*_{\|s} \cdot \mathbf{b}$ corresponds to the volume element in guiding center velocity, with $\mathbf{B}^*_{\|s} \equiv \mathbf{B} + \frac{m_s}{q_s} v_{g\|} \nabla \times \mathbf{b}$ and $\mathcal{R}hs$ is the right-hand side:

$$\mathcal{R}hs \left(\bar{F}_s \right) = B^*_{\|s} \left(\mathcal{D}_r \left(\bar{F}_s \right) + \mathcal{K}_r \left(\bar{F}_s \right) + \mathcal{C}_r \left(\bar{F}_s \right) + \mathcal{S} \right) \tag{2.2}$$

where $\mathcal{D}_r$ is the diffusion term that represents the process by which particles spread out in space or velocity space due to random motion, often resulting from collisions or other interactions. $\mathcal{K}_r$ is the Krook operator that is a simplified model for collisions that approximates the effect of collisions by driving the distribution function F towards a Maxwellian equilibrium distribution over time. $\mathcal{C}_r$ is the collision operator that describes the detailed effect of collisions between particles, modifying the distribution function based on interactions like scattering, energy exchange, and momentum transfer. $\mathcal{S}$ is the source term, that accounts for any external sources of particles, such as injection, ionization, or other processes that add particles to the distribution function F.
In GYSELA, we are limited to 3 distribution functions, one describing electrons, so it is only possible to depict two other ions. Which can be deuterium and tritium or a main species plus an impurity of various types, which can be intrinsic (i.e. those coming from within the plasma core such as helium) or extrinsic (that come from the materials of the tokamak and inevitably enter the plasma through various mechanisms, such as erosion of the tokamak walls and internal components, such as tungsten).

ii) Set of four coupled ordinary differential equations (ODE) for the trajectories:

$$\frac{\mathrm{d}x^i_G}{\mathrm{d}t} \;=\; v_{G\|}\mathbf{b}^*_s \cdot \nabla x^i_G \;+\; \mathbf{v}_{E\times B_s} \cdot \nabla x^i_G \;+\; \mathbf{v}_{D_s} \cdot \nabla x^i_G \tag{2.3}$$

$$m_s\frac{\mathrm{d}v_{G\|}}{\mathrm{d}t} \;=\; -\mu_s \mathbf{b}^*_s \cdot \nabla B \;-\; q_s \mathbf{b}^*_s \cdot \nabla\bar{\Phi} \;+\; \frac{m_s v_{G\|}}{B}\mathbf{v}_{E\times B_s} \cdot \nabla B \tag{2.4}$$

where $\mathbf{b}^*_s = \frac{\mathbf{B}}{B^*_{\|s}} + \frac{m_s v_{G\|}}{q_s B^*_{\|s} B}\nabla\times\mathbf{B}$.
It is possible to split 2.3 by components:

- the ith contravariant component of $\mathbf{b}^*_s$ is:

$$\mathbf{b}^*_s \cdot \nabla x^i_G \;=\; \mathbf{b}^{*i}_s \;=\; \frac{\mathbf{B}\cdot\nabla x^i}{B^*_{\|s}} \;+\; \frac{m_s v_{G\|}}{q_s B^*_{\|s}}\frac{\mu_0 \mathbf{J}\cdot\nabla x^i_G}{B} \tag{2.5}$$

  where $\mathbf{J}$ is the current,
- the ith controvariant component of the $'\mathbf{E}\times\mathbf{B}'$ drift are given by:

$$\mathbf{v}_{E\times B_s} \cdot \nabla x^i_G \;=\; \mathbf{v}^i_{E\times B_s} \;=\; \frac{1}{B^*_{\|s}}\left[\bar{\Phi}, x^i_G\right] \tag{2.6}$$

  where $[F,G] = \mathbf{b}\cdot(\nabla F \times \nabla G)$ are the Poisson bracket,
- and the ith contravariant components of the 'grad-B' and 'curvature' drifts are:

$$\mathbf{v}_{D_s} \cdot \nabla x^i_G \;=\; v^i_{D_s} \;=\; \left(\frac{m_s v^2_{G\|} + \mu_s B}{q_s B^*_{\|s} B}\right)\left[B, x^i_G\right] \tag{2.7}$$

iii) a 3D integro-differential equations for the field know as *quasi-neutrality* or *Poisson equation*:

$$-\frac{1}{n_{e0}}\sum_s Z_s \nabla_\perp \cdot \left(\frac{n_{s0}}{B_0\Omega_S}\nabla_\perp\Phi\right) + e\left(\frac{\Phi - \langle\Phi\rangle_{FS}}{T_e}\right) \;=\; \frac{1}{n_{e0}}\sum_s Z_s\left(n_{G_s} - n_{G_s,eq}\right) \tag{2.8}$$

where n_{e0} is the initial electron density, Z is the atomic number, n_{s_0} is the initial radial density profile„ B_0 is the initial magnetic field, $\Omega_s = q_s B_0/m_s$ is the cyclotron frequency (it is the corresponding of eq 1.10, but generalized for all the species), $\nabla_\perp = \left(\delta_r, \frac{1}{r}\delta_\theta\right)$, $\langle\Phi\rangle_{FS}$ represent the flux surface average, T_e is the electron temperature, n_{G_s} is the gyro-center density of species s and $n_{G_s,eq}$ is the gyro-center density for $\bar{F} = \bar{F}_{s,eq}$.
The right hand side of 2.8 is the charge density of the guiding-center ρ and is described by:

$$\rho(\mathbf{x},t) = \frac{1}{n_{e_0}}\sum_s Z_s \int d\mu \mathcal{J}_\mu \cdot \left[\int J_V dv_{G\|}\left(\bar{F} - \bar{F}_{s,eq}\right)\right] \tag{2.9}$$

where $\mathcal{J}$ is the gyro-average operator and J_V stand for the Jacobian in the velocity space.

iv) and the *Ampere equation*:

$$-\frac{1}{\mu_0}\nabla^2_\perp A_\| \;+\; \sum_s \frac{n_o e^2}{m_s}A_\| \;=\; \sum_s u\bar{\Phi}\left[\bar{F}B^*_\|\right]\mathrm{d}u\mathrm{d}\mu - \sum_s e\int \mu\bar{\Phi}\left[\bar{F}B^*_\|\right] \tag{2.10}$$

2.2.1 Poisson solver in GYSELA

In this section is presented a brief introduction to how the Poisson equation 2.8 is solved within GYSELA; this introduction will be useful in the continuation of this work. To solve the Poisson equation let define the Poisson solving operator $\tilde{\mathrm{Q}}$ that denotes symbolically four steps [24]:

i) Computing the right-hand side of the quasi-neutrality equation 2.8 using 2.9,

ii) solving the quasi-neurality equation 2.8 to deduce the electrostatic potential Φ,

iii) compute the gyro-averaged electric potential $\bar{\Phi} = \mathcal{J}_\mu \Phi$

iv) compute the electric field $\mathbf{E} = \nabla\bar{\Phi}$

Inside the GYSELA algorithm, the Poisson solver $\tilde{\mathrm{Q}}$ is inside a subroutine named: *QN_solver _solve*, that is called at each time step for computing the electrostatic potential Φ_{t_n+1}. There are 3 models available in GYSELA to describe the behaviour of electrons: adiabatic, trapped-kinetic and full kinetic. In the first case, all electrons are treated by assuming that their responses are rapid with respect to fluctuations in the electromagnetic field and that they adapt instantaneously to changes in potential. This model offers a significant simplification for rapid analysis. In the second case, passing electrons are treated as adiabatic, while trapped electrons (i.e. those that do not make a complete revolution around the magnetic field line and instead oscillate between two reflection points) require a more detailed kinetic treatment. In the latter case, both trapped and passing electrons are treated as fully kinetic. This approach makes no distinction between the different electron motion regimes and offers a more complete and accurate description. For each of these, there is a different *Poisson_solver* subroutine. Without going into the details of the mathematical and numerical descriptions of the 3 models, during this work, we will use the Poisson solver for the full-kinetic description.

GYSELA's global algorithm, in particular the coupling between the Vlasov, Poisson and Ampere solving is shown in figure 2.1, for more detail about that refer to [24].

For a brief introduction to the variables involved, let us denote the number of ion species by N_{species} and the number of μ values by N_μ (Since the magnetic moment μ is an adiabatic invariant, it acts as a parameter). Consequently, for each species, we need to solve N_μ independent Boltzmann equations (Equation 2.1). Let N_r, N_θ, N_ϕ, and $N_{vG\|}$ represent the number of points in the r, θ, ϕ, and $v_{G\|}$ directions, respectively. The GYSELA code uses large data structures, including 5D data of size $N_r \times N_\theta \times N_\phi \times N_{vG\|} \times N_\mu$ for distribution functions and 3D data of size $N_r \times N_\theta \times N_\phi$ for the electrostatic potential Φ, its derivatives and the parallel component of the vector potential $A_\|$, as well as for the first moments of the distribution function. These quantities and data are saved so that they can be studied by specially developed post-process diagnostics. Diagnostics written in Python were used during this work, and other diagnostics were developed for more detailed studies.

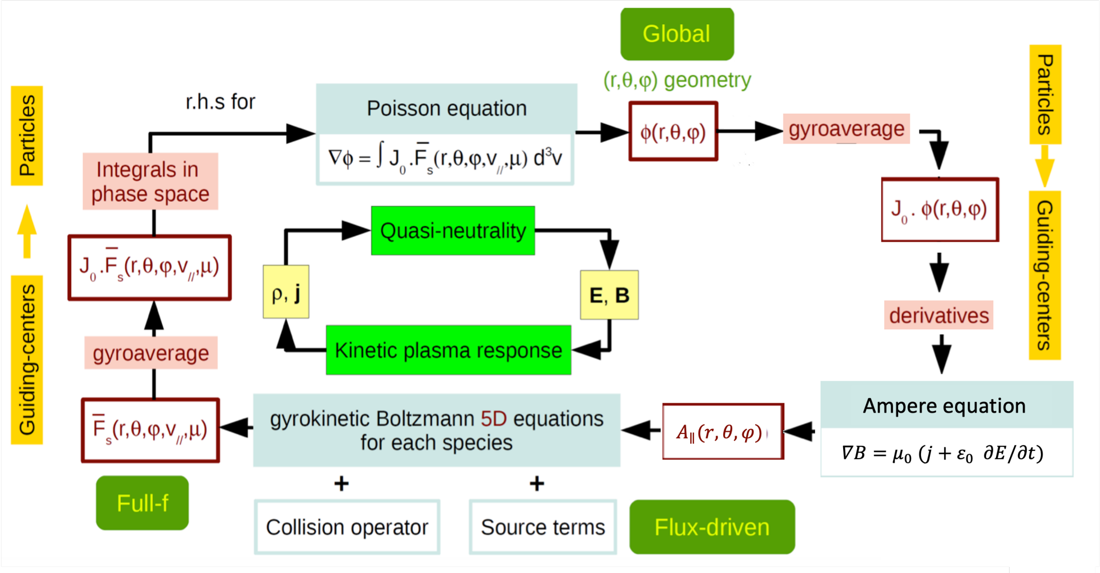

Figure 2.1: *Schematic view of the coupling between the Vlasov, Poisson and Ampere solvers in GYSELA, adapted from [24].*

Chapter 3

Alfvén eigenmodes in GYSELA

The linear calculation of fast particle-driven TAE dynamics has been well studied, analysed and benchmarked in various code [27] but never using a semi-Lagrangian non-linear global and full-f gyro-kinetic code (like GYSELA). To study the dynamics of TAEs in GYSELA, this work follows the studies that *Zhang et al.* [28] had done with global gyrokinetic toroidal cote GTC and what *Biancalani et al.* [29] and *Sadr et al.* [30] had done using the global gyrokinetic particle-in-cell code ORB5.
GTC, as the name indicates, is a global gyrokinetic code, is a code based on the Particle-in-cell (PIC) approach and uses a δf configuration [31]. ORB5 is also a gyrokinetic code that uses a particle-in-cell PIC approach, and for the study of Alfvén Eigenmodes uses a $\delta - f$ approach, (although it is possible to use the code as a $full - f$) [32].

In this chapter is introduced the work that has been carried out on GYSELA. It will begin by presenting the results obtained using a cylindrical configuration to reproduce the continuum, and then move on to a more realistic toroidal configuration to try to observe the opening in the gap in the continuum (see section 1.3).
This work is in continuity with studies carried out by David Zarzoso Fernandez (a researcher a Centre Nationale de la Recherche Scientifique - CNRS in Marseille) on the same topic.

3.1 Continuum spectrum in a cylinder

In this section, we present the outcomes of GYSELA tests focusing on the simplest plasma confinement configuration: the cylindrical geometry. This is accomplished by selecting analytical magnetic equilibria characterized by a very big aspect ratio: $A = 100$ (eq. 1.4). Numerical simulations are conducted featuring flat q profiles (eq. 1.6). Establishing an initial perturbation, let evolve the plasma over time and measure the SAW oscillation frequency across various values of q, electron mass and electron beta $\beta = \mu_0 p_e / B^2$. This frequency represents the inherent oscillation frequency of the plasma and is referred to as the continuous spectrum, or simply continuum [8].

For this study, is chosen an analytical equilibrium with a value of $\beta = 2 \times 10^{-4}$ and

$\rho^* = \rho_s/a = 1/50$, with $\rho_s = c_s/\omega_{C0}$ being the sound gyroradius, $c_s = \sqrt{T_e/m_i}$ being the sound speed and ω_{C0} the ion cyclotron frequency [eq. 1.10]. A flat temperature and density profile was selected with the ratio of electron to ion temperature $\tau = 1$ (for all simulations presented in this work). The time step $dt = 1\omega_{c0}$ of the simulation was and the spatial resolution $(N_r, N_\theta, N_\varphi) = (64, 64, 32)$, that is the same spatial resolution used by *Biancalani et al.* [29] to study this phenomenon and a typical spatial resolution of simulation with $\rho^* = 1/50$ in GYSELA.
For all the simulations carried out, it was decided to study the collisionless case without any density or temperature gradients. Gradients are set to zero to avoid the formation of turbulence and micro-tearing modes. The collisionless approach is justified since GYSELA's electron-ion collision operator has not been benchmarked with the actual mass ratio [26], as is done in some of the simulations for this internship.

Note that normalisation in GYSELA is done by the ion cyclotron frequency, so the time and the time-step Δt is expressed as the inverse of this frequency ($\Delta t = \omega_{c0}^{-1}$). The Alfvén velocity normalised according to the ion cyclotron frequency is: $v_A = \frac{\rho^* R}{A\sqrt{\beta}}$ and consequently equation 1.19 normalised according to GYSELA normalization becomes:

$$\omega^2_{SAW} = \frac{\rho^{*2}}{\beta A^2} \cdot \frac{(m - nq)^2}{q^2} \, [\omega_{c0}] \tag{3.1}$$

It should be noted that in comparison to the GTC code [28] [33] and ORB5 [30], the β_e (or simply β in the remainder of this thesis) value in GYSELA is defined differently, in GTC and ORB5 $\beta_e = \frac{8\pi n_e T_e}{B_0^2}$, while in GYSELA $\beta_e = \frac{4\pi n_e T_e}{B_0^2}$, this leads to discrepancies in the normalisation according to ω_{c0}. In fact, during the simulations carried out by GYSELA, a β value was used which does not correspond to the β value of the ITPA refernece case.

3.1.1 Alfvén continuum

To study the Alfvén continuum were conducted simulations for non-axisymmetric perturbations. The same magnetic equilibrium profile, plasma temperature, and density as described in Sec. 3.1 are considered. Namely the simulations were carried out with $\beta = 2 \times 10^{-4}$, $\rho = 50$ and mass ratio $m_i/m_e = 2000$. Multiple simulations are performed, each with a different value of q and a flat q profile. A perturbation is initialized with amplitude 10^{-3} with toroidal mode number $n = 2$ and poloidal mode number $m = 4$ and after with $n = 2$ and $m = 5$. The simulations are evolved in time (note that only the poloidal mode $n = 2$ is evolved) and the evolution of the mode in the middle of the radial domain ($r/a = 0.5$) is analyzed. From the timetrace of the parallel component of the magnetic vector potential $A_\parallel$, an oscillation in the amplitude signal is observed (see Fig. 3.1) and, through a Fourier analysis on time, it is calculated the frequency of this oscillation.

Several simulations with different values of q are carried out and the scan in frequency is compared with the ideal MHD prediction (1.20). A good match is observed for both modes $m = 4$ and $m = 5$, in the cylindrical limit (1.19) as reported in figure 3.2.

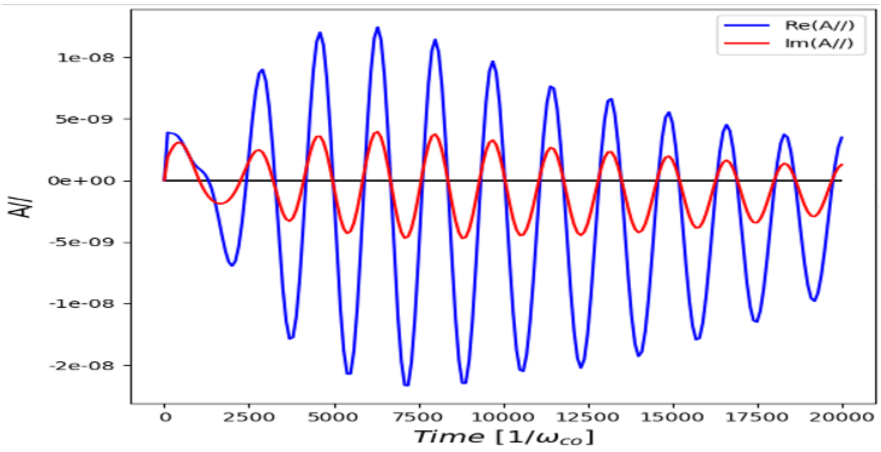

Figure 3.1: *Timetrace of the real and imaginary part of the mode* $n = 2$ *and* $m = 4$ *of parallel component of the magnetic vector potential* $A_{\parallel}$ *for* $q = 2.3$*. An oscillatory damping trend is observed. The frequency of this oscillation is calculated.*

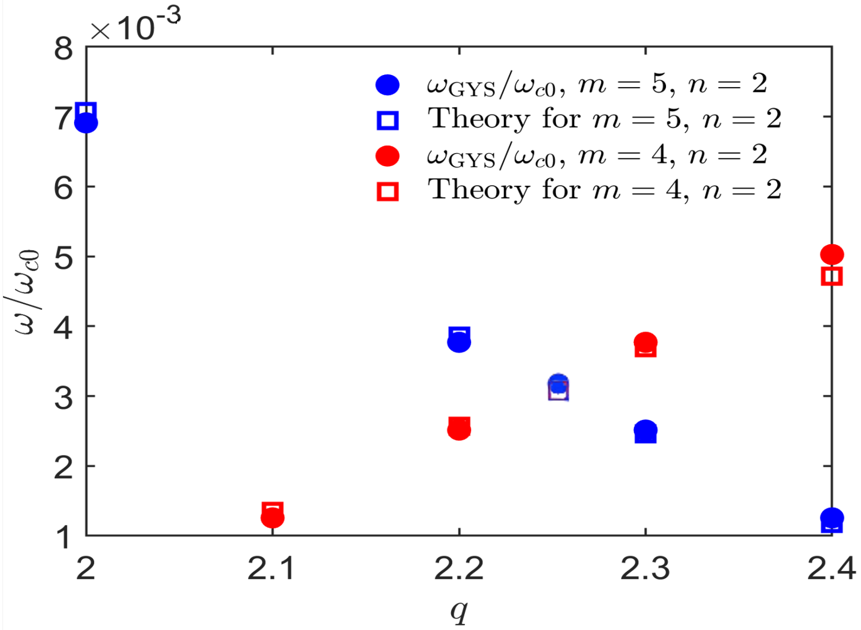

Figure 3.2: *Frequency (normalized to the ion cyclotron frequency* ω_{C0}*) dependency on* q *for different simulations with flat* q *profiles and with the evolution in time of only one poloidal component (*$m = 4$ *or* $m = 5$*) and toroidal mode number* $n = 2$*. In this analysis, the cylinder limit (*$A = 100$*) is considered. A good match with the MHD theory is observed. Note that for* $q = 2.25$ *the frequency obtained from the simulations for the mode* $m = 4$ *and* $m = 5$ *are the same.*

As anticipated in Sec. 1.3.1, within this cylindrical limit, no gap in the continuum spectrum attributable to toroidicity is observed at the intersection of the two branches. However, the

introduction of toroidal curvature, achieved by decreasing the aspect ratio A, leads to the formation of a gap (as can be clearly seen in figure 1.11 above).
The following section performs simulations with considerable toroidal curvature (that cannot be neglected in equation 1.20).

3.2 Toroidicity-induced Alfvén eigenmode

In this section, we examine a more realistic scenario by considering a smaller value of the aspect ratio, thereby introducing greater toroidal curvature. Consequently, in this configuration, as explained in section 1.3.1, a gap in the continuous spectrum emerges at the intersection of two adjacent cylinder branches, denoted as m and $m + 1$ (figure 3.3). Moreover, it may induce a global eigenmode with a frequency lying within the continuum gap (the TAE previously explained).

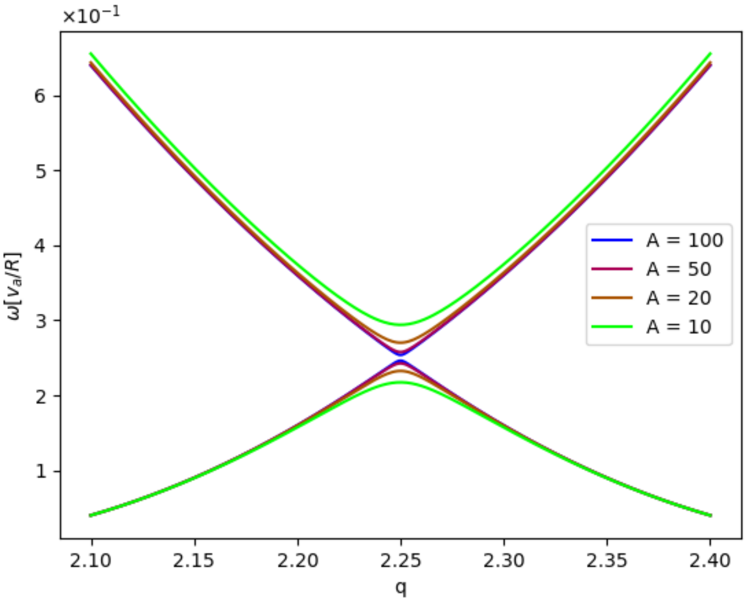

Figure 3.3: *Plot of the continuum spectra (eq.1.20 for* $n = 2$ *and* $m = 4$ *and* $m = 5$ *normalized to* v_a/R *for various aspect ratios (A = 100, 50, 20, 10). The parameters are the one of our simulations (*$\rho^* = 1/50,\ \beta = 2 \times 10^{-4}$*). Note that as the aspect ratio A decreases, there is an increase in the gap in the continuum. For* $A = 100$ *and* $A = 50$*, this gap is negligible, as the gap corresponds to frequencies in the order of* $10^-5\omega_{c0}$*. Which become in the order of* $10^{-4}\omega_{c0}$ *for* $A = 20$ *and in the order of* $10^{-3}\omega_{c0}$ *for* $A = 10$*, the same order of magnitude of the SAW frequency, thus no longer neglectable.*

In the toroidal configuration, we performed the same analyses as in the cylindrical configuration: initialize a perturbation with amplitude 10^{-3} with toroidal mode number $n = 2$ and poloidal mode number $m = 4$ and after with $n = 2$ and $m = 5$, let evolve on time the simulation and analyze the evolution of the mode with $n = 2$ and $m = 4$ and subsequently with same $n = 2$ and $m = 5$ in the middle of the radial domain ($r/a = 0.5$). The same parameters used are flat profiles for q, density, and temperature, $\rho^* = 1/50$ and $\beta = 2 \times 10^{-4}$. From studying the parallel component of the magnetic vector potential $A_\parallel$ for the mode $n = 2$ and $m = 4$, it can be seen in figure 3.4 that as the aspect ratio decreases (gradually going from $A = 100$ to $A = 10$), there is no longer a clear dominant oscillatory structure and a dominant damping frequency.

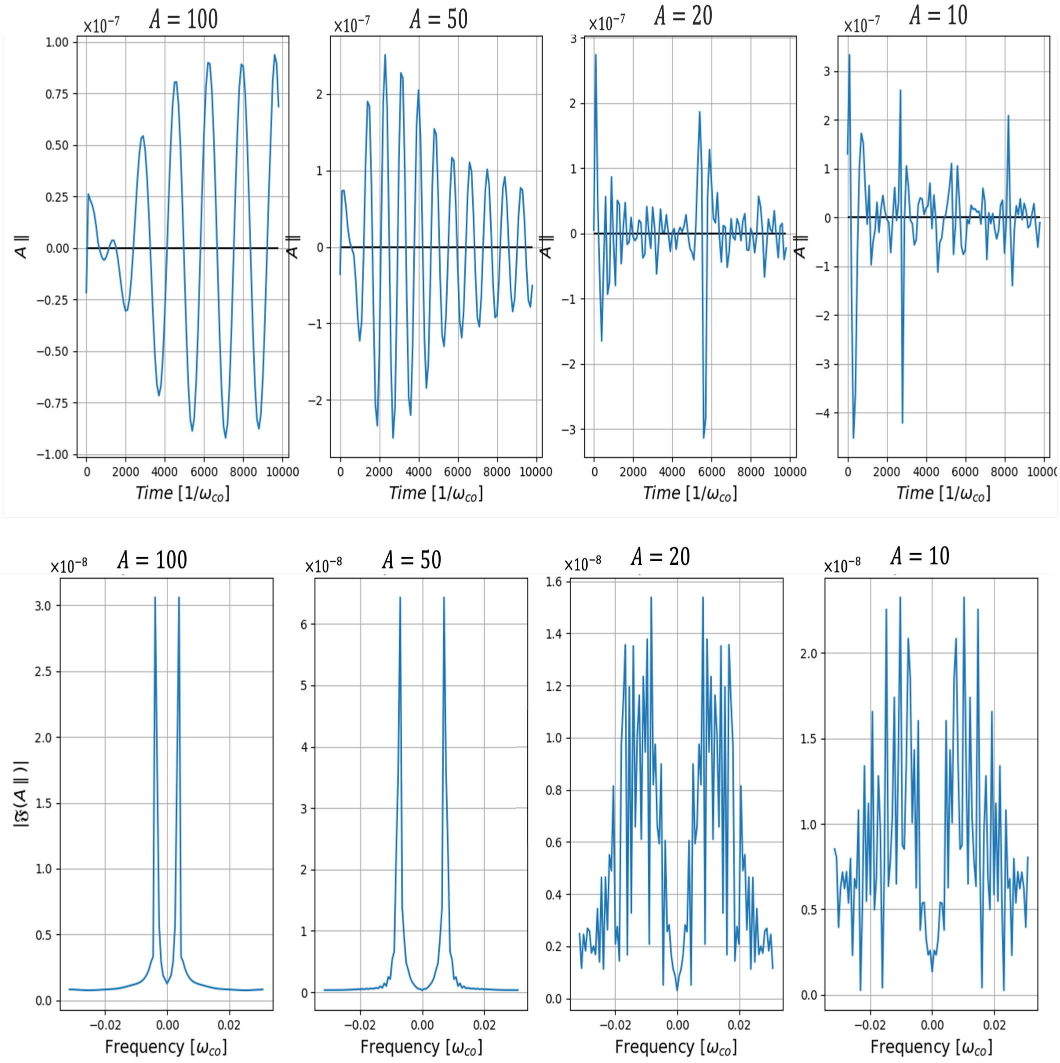

Figure 3.4: *Plot of the timetrace (up) and the corresponding Fourier spectra (down) for the mode* $n = 2$ *and* $m = 4$ *of the parallel component of the magnetic potential* $A_\parallel$ *for* $q = 2.25$. *From the Fourier spectra (down) result evident the absence of a clear dominating damping frequency with the decreasing of the aspect ratio.*

From the analysis of a poloidal section (figure 3.5) (taken at the position $\varphi = 0$) of $A_{\|}$ in the case with aspect ratio $A = 10$, it is evident the predominance of the mode $m = 4$ and $m = 5$ over the others. At $t = 5000\omega_{C0}^{-1}$ the mode $m = 5$ is predominant in the outer region and in the center of the section. At $t = 10000\omega_{c0}^{-1}$ the predominant one is the mode $m = 4$ located near the boundary.

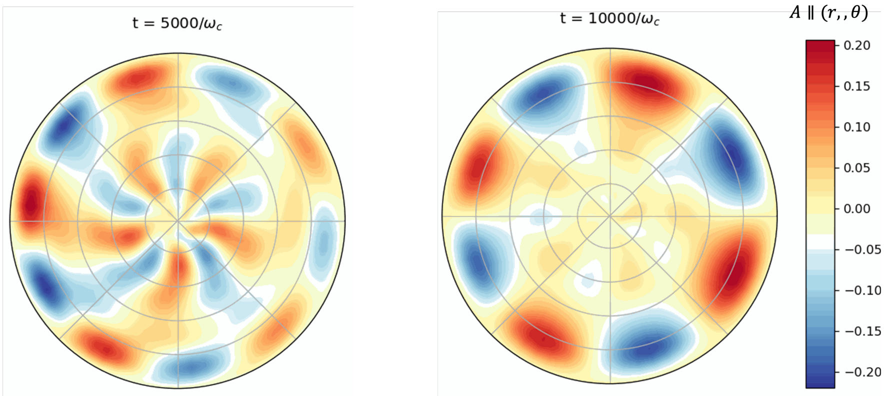

Figure 3.5: *Poloidal section, taken at position* $\varphi = 0$ *of* $A_{\|}$ *for aspect ratio* $A = 10$ *at time* $t = 5000/\omega_{C0}^{-1}$ *(left) and* $t = 10000/\omega_{C0}^{-1}$ *(right). It is evident the predominance of the mode* $m = 4$ *and* $m = 5$ *over the others and the presence of higher-intensity modes near the edges of the domain.*

The presence of higher-intensity modes near the edges of the domain is a potential indicator of problems. This is because in GYSELA the Dirichlet condition is applied at the edge of the radial domain, in particular, the electrostatic potential Φ is forced to zero at the most extreme point of the radial domain: $\Phi(r = N_r, \theta, \varphi) = 0$. This can lead, close to the edge, to artificially induced phenomena of this imposition and not inherent plasma ones.

In order to solve this problem, the first step we took was to enlarge the domain to allow the modes space to grow. This is achieved by decreasing the value of ρ^*, then increasing the minor radius a. In GYSELA, the minor radius is expressed in Larmor radius value, which means that the increase of a means means increasing the number of Larmor radii in our radial domain. In order to actually study a wider domain, we must also enlarge the resolution, namely the number of grid points $(N_r, N_\theta, N_\varphi)$. This was done taking into account that the simulations presented above were carried out using a fairly large ρ^* value ($\rho^* = 1/50$), whereas the international cross-code reference test case 'ITPA-TAE' [27] utilises parameters that correspond to a value of $\rho^* = 1/927$ in toroidal configuration. There are two main problems with the increase of the radial domain. The first one is the increased computational costs required as using a larger mesh means processing more points, thus requiring more computational time to achieve the same plasma time. The second is a problem concerning frequencies. As mentioned earlier, normalisation in GYSELA is performed using the cyclotron frequency, resulting in the eq. 3.1 for the frequency of the SAW. In Eq. 3.1, ρ^* is at the numerator, so a decrease of the value of ρ^* involve a consequent decrease in the oscillation frequency of the modes we want to analyse. This leads to longer simulations having to be carried out in order to detect these frequencies, which further increases the computational

cost.
In particular, analyses were carried out with $\rho^* = 1/150$ with a resolution of size $(N_r, N_\theta, N_\varphi) = (256, 256, 64)$. During the analysis, it was noted that the number of radial points was excessive in relation to the value of ρ^*, so, for computational reason, it was decided to decrease the number of mesh points by increasing ρ^*, performing simulations with $\rho^* = 1/400$ with resolution of $(N_r, N_\theta, N_\varphi) = (128, 128, 32)$. In the latter case, the simulation ran for more than $150000\omega_{c0}^{-1}$. In none of these simulations was observed a significant improvement in the results, and no clear structure with a dominant damping frequency as in the figures was ever notice.

In the paper of *Biancalani et al.* [29] moving from a cylindrical to a toroidal configuration $(A = 10)$, a mass ratio $m_i/m_e$of 200 is used instead of 2000. This mass ratio value is also used in the reference paper for TAEs [27] and in [30], so we perform simulations with $m_i/m_e$of 200, with $\rho^* = 1/50$ and resolution of $(N_r, N_\theta, N_\varphi) = (64, 64, 32)$ and $\rho^* = 1/150$ with $(N_r, N_\theta, N_\varphi) = (256, 128, 32)$.In [27], in [29] and [30], a parabolic q profile is used in the case of simulations in a toroidal configuration, and not a flat one as in the simulations in a cylindrical case. The q profile is $q(r) = 2.2 + 0.2(r/a)^2$. With this q profile, we have that the value of q corresponding to the intersection between the two branches of the continuum that couple ($n = 2$ with $m = 4$ and $m = 5$ that give rise to the gap in the continuum is $q = 2.25$ and it is in the middle of the radial domain. We performed a simulation with this parabolic q profile in the case with $\rho^* = 1/400$. Also with these parameters, no improvements were noted.

As a further improvement, we used the same parameters as in the reference test case [27], where the q profile is profile $q(r) = 1.71 + 0.16(r/a)^2$ and in the middle of the radial domain $q = 1.75$. Using this profile, there is a toroidal Alfvén eigenmode with toroidal mode $n = 6$ and poloidal mode number $m = -10$ and $m = -11$. In addition, with this q profile there is another TAE gap mode with $n = 2$ and $m = -3$ and $m = -4$. (see Fig. 3.6). In this case we have $\beta = 9.1 \times 10^{-4}$ and parameters corresponding to $\rho^* = 1/927$. The resolution chosen to study this case in our code was $(N_r, N_\theta, N_\varphi) = (256, 256, 64)$. With these parameters, the TAE frequency for the ITPA case, normalised to the cyclotron frequency was found to be $\omega_{gap} = 0.280995\omega_A = 0.001532\omega_{c0}$, requiring a simulation time of at least $10^5\omega_{c0}^{-1}$. This factor together with the large resolution and domain made this simulation computationally very heavy. We were therefore only able to run it for $10000\omega_{c0}^{-}1$, but even in this case, no oscillatory trend with a clear damping frequency was observed.

Despite these various attempts with different parameters and configurations, we were not able to identify the gap in the continuum through GYSELA. This may be due to various factors: the gap may be hidden by other phenomena (which we have not studied) that are generated as the toroidicity increases; it may be that we have not found the right set-up for the numerical parameters to allow the detection of this phenomenon; or it might be due to other elements that we have not considered. We also noticed that no codes in similar configurations (i.e. global gyrokinetic codes) [27], [29], [30], and [33] show the gap in the continuum, so we decided to move on to the next step: exciting the modes in the gap of the continuum

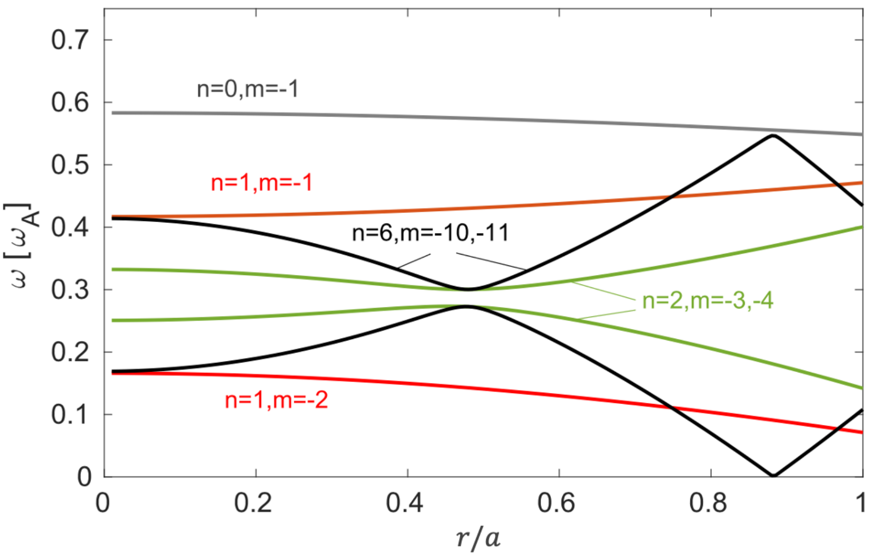

Figure 3.6: *Alfvén continua of ITPA case for n = 0,1,2,6 and seven toroidal mode numbers. It is possible to see the TAE gap due to the coupling between the mode with n = 2 with m = -3 and m = -4 and the one due to the coupling between the mode with n = 6 and m = - 10 and m = - 11. Note that here the normalization for the frequency is done using the Alfvén frequency, not the ion cyclotron frequency so it is independent from the choice of the simulation parameters. From [30]*

Chapter 4

Destabilization of Toroidal Alfvén eigenmode in GYSELA through an external antenna

In this chapter, we are going to illustrate the approach chosen to excite the modes in the gap in the continuum.

As explained in section 1.3, the Alfvén velocity is in the same order of magnitude as the characteristic velocities of fast ions. So fast ions can interact with Alfvèn waves and this can lead to an energy transfer and the excitation of instabilities. In particular, it was explained that perturbations with frequencies within the gap of the continuum are not damped. To study this phenomenon in GYSELA, the first option that was considered was to introduce fast ions into the code. Doing that means introducing a new species with the same mass of the thermal ions in GYSELA but at different (higher in this case) energies. However, this poses a huge problem in the energy grid, because normalisation in GYSELA is done through the scalar $\tau = \sqrt{T_r/m_s}$, where T_r is the reference temperature for each species and m_s is the mass of the species. Thus introducing a species with the same mass would have implied writing τ as a vector, which would have implied implementing very deep and structural changes in the code. Hence an alternative option was chosen: to excite the modes in the continuum gap through an antenna. This choice is well tested and benchmarked in other codes, notably in GTC in the work done by *Zhang et al.*[28] and by *Aslanyan et al.* [33]. In particular, in that work was imposed a perturbation in the electrostatic potential Φ_{ant} that is added to the plasma electrostatic potential Φ_{plasma} resulting in: $\Phi = \Phi_{plasma} + \Phi_{ant}$. In ORB5, *Sadr et al.* [30] introduces an electromagnetic antenna that perturbs both the electrostatic potential ($\Phi = \Phi_{plasma} + \Phi_{ant}$) and parallel component of the magnetic vector potential ($A_{\parallel} = A_{\parallel,plasma} + A_{\parallel,ant}$). For now, as a first approach to the code and to the problem, it was decided to implement the antenna as a perturbation only in the electrostatic field in GYSELA.

The idea of inserting an antenna that perturbs the plasma has been investigated both through numerical simulations and also during experimental studies conducted within tokamaks. For

example, in the Joint Europen Tokamak (JET), there is a diagnostic dedicated to the study of Alfvén eigenmode: the Alfvén Eigenmode Active Diagnostic (AEAD) system [34] [35] [36]. In the JET, eight in-vessel antennas (marked with the red box in figure 4.1 in the left panel) were installed to actively investigate stable Alfvén Eigenmodes (AEs) with frequencies between 25 and 250 kHz and toroidal mode numbers $|n| < 20$ [36]. The destabilisation occurs by using variable frequency waves generated by these antennas that perturb the plasma. This system uses magnetic probes that provide a real-time spectrogram of the plasma's response to the induced perturbation. A perturbation is damped everywhere except when a gap is present in the continuum. So if a perturbation has frequency in the gap, an increase in intensity will be observed in the signal measured by the magnetic probes. The objective is therefore to vary the frequency of the perturbations generated by the antenna in the range where there are present gaps in the continuum and, when the magnetic probes detect an increase in intensity, an attempt is made to follow this perturbation with the perturbation imposed by the antenna. A stable AE was tracked in real-time during the high-heating power phase when both the Ion Cyclotron Resonance Heating (ICRH) and the Neutral Beam Injection (NBI) were active. This can be seen in the Fourier decomposition of magnetic signals in figure 4.1 in the right panel. The triangular waveform is the scanning AEAD frequency, (with frequency$f$ between 125 and 250 kHz. Around $t = 11s$, a stable AE is detected by the AEAD at $f_0 \sim 245kHz$ (highlighted with the orange box), and the real-time monitoring system quickly changes the scan direction to track the mode until $t \sim 12s$ [36].
Various examples of TAE destabilisation by an external antenna are given in the literature ([34], [35] and [36])

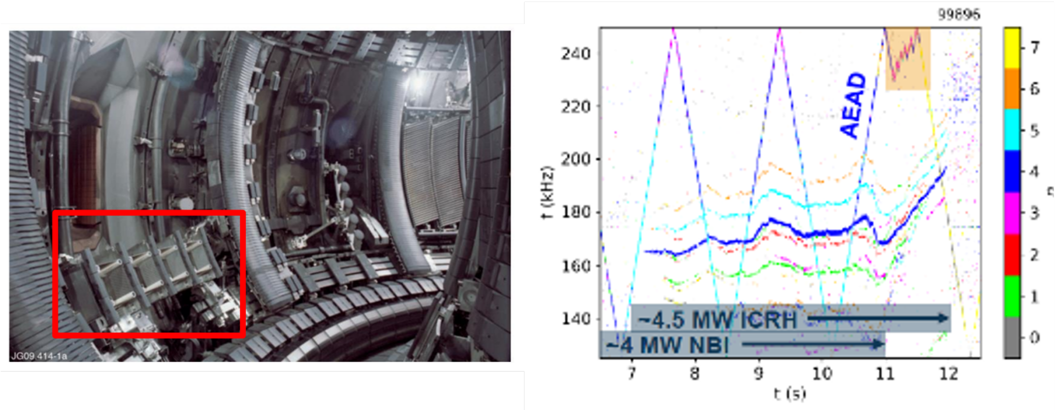

Figure 4.1: *View of one assembly of 4 antennas, as installed on the low-field-side wall of the JET vessel [34]. Spectrogram of Fourier decomposition of magnetics data from the Alfvén Eigenmode Active Diagnostic (left-bottom quadrant) with toroidal mode number analysis (Right side). In the orange box at the top right, you can see the antenna's attempt to follow the increase in intensity detected by the magnetic probes. From [36]*

4.1 Electrostatic antenna

As explained above, the aim of this thesis is to excite the modes in the continuum gap via an electrostatic antenna. This antenna imposes a perturbation Φ_{ant} that adds to the electrostatic plasma potential Φ_{plasma}, resulting in a total electrostatic potential: $\Phi = \Phi_{plasma} + \Phi_{ant}$.
To excite the TAE mode, in all the analysed papers ([29], [30] and [28]), the electrostatic antenna simultaneously excites the 2 coupled modes that lead to the formation of the gap. The only reference in which the antenna equation is written explicitly is the one on ORB5 by *Sadr et al.* [30]. An analogous electrostatic antenna potential equation will be used for the tests in this work. As explained in Section 3.2 and seen in Figure 3.6, in the ITPA case there, for that particular frequencies there are two overlapping gaps in the continuum, one due to the coupling between modes with $n = 6$ and $m = -10$ and $m = -11$ and the one with $n = 2$ and $m = -3$ and $m = -4$. During this thesis, for computational and time reasons, as a first approach to the problem only the TAE due to the coupling with $n = 2$ and $m = -3$ and $m = -4$ was excited.

Hence we consider an antenna with $\tau = \{(n_1,\ m_1),\ (n_2,\ m_2)\} = \{(2,-4),(2,-3)\}$ and a gaussian radial profile:

$$h_j(r) \;=\; a_j e^{\frac{-(r-r_{0,j})^2}{\delta_i^2}} \quad for\ i = 1,2 \tag{4.1}$$

where:

$$a_1 = a_2 = 0.1, \quad r_{0,1} = r_{0,2} = 0.5, \quad \delta_1 = \delta_2 = 0.1 \tag{4.2}$$

where a_i is the amplitude of the Gaussian radial profile, r_i its mean and δ_i its variance.
The equation of the electrostatic potential of the antenna is:

$$\Phi_{ant}\left(r,\theta,\varphi,t\right) \;=\; \Re\left[\sum_{j=1}^{2} h_j(r) e^{i(m_j\theta+n\varphi)e^{i\omega_{ant}t}}\right] \tag{4.3}$$

with ω_{ant} the frequency of the antenna.
A representation of the poloidal and toroidal cross-section of the electrostatic antenna for the mode $n = 2$ with $m = -3$ and $m = -4$ is shown in figure 4.2.

Before examining how the equations are implemented in the code, it is possible to rewrite the equation 4.3 in the form:

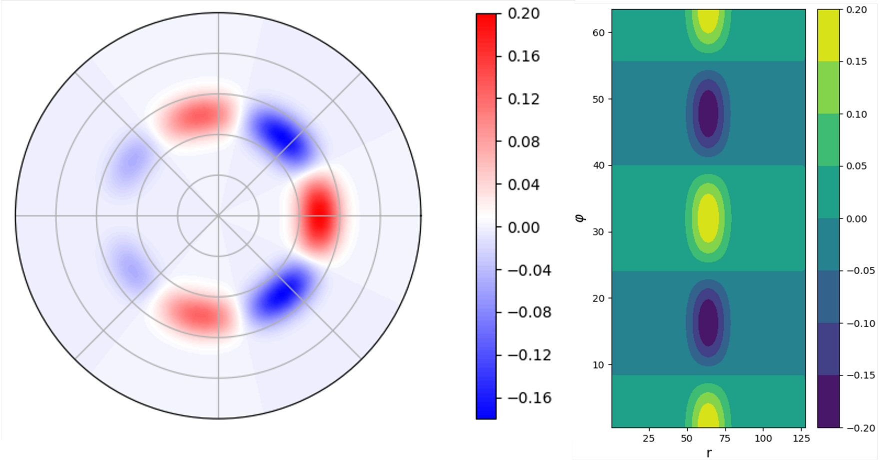

Figure 4.2: *Poloidal (left) and toroidal (right) cross-section of the electrostatic antenna Φ_{ant} at $t = 0$. To note the overlap between the modes $m = -3$ and $m = -4$, and how the antenna is centred in the middle of the radial domain.*

$$\begin{aligned}\Phi_{ant}\left(r,\theta,\varphi,t\right) &= \underbrace{\left[\sum_{j=1}^{2} h_j(r)\cos(m_j\theta + n\varphi)\right]}_{:=\, S_{ant,1}(r,\theta,\varphi)} \cdot \cos(\omega_{ant}t) \\ &\quad + \underbrace{\left[\sum_{j=1}^{2} h_j(r)\cos(m_j\theta + n\varphi + \frac{\pi}{2})\right]}_{:=\, S_{ant,2}(r,\theta,\varphi)} \cdot \sin(\omega_{ant}t)\end{aligned} \tag{4.4}$$

By doing this, we have decomposed the equation into four parts: two spatial parts $S_{ant,1}$ and $S_{ant,2}$, dependent only on (r, θ, φ), and two time-dependent parts. This allows for a simpler and more computationally effective implementation within the code, as the two spatial parts can be computed only once at the beginning of the simulation and called up later at each time step when calculating the total antenna electrostatic potential.

4.2 Implementation of the antenna in GYSELA

Referring to what is expressed in paragraph 2.2.1, the operator solving the Poisson equation (eq.2.8) consists of 4 steps. The antenna is inserted between step ii) and step iii), namely after the code has calculated the electrostatic potential of the plasma and before performing the gyro-averaged operation (fig. 4.3).

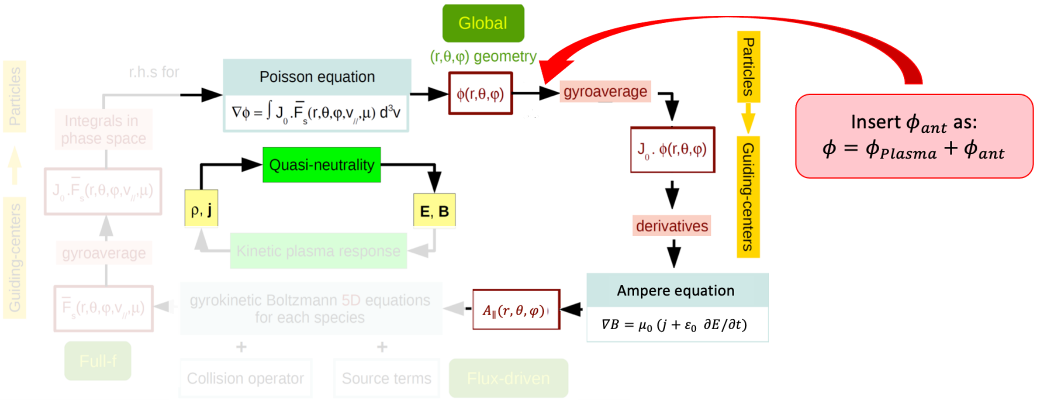

Figure 4.3: *Schematic view of antenna integration inside GYSELA, adapted from [24]*

.

4.2.1 Implementations in the code

The insertion of the antenna required modifications inside the routine that solve the Poisson equation: `QN_solver_solve`. As mentioned in paragraph 2.2.1 only the Poisson Solver for the full-kinetic electron is modified (in particular the routine `QN_FKE_solve` inside the file `QN_fullkin_elec.F90`). In this section, we will present all the modified files and routines to implement the antenna inside GYSELA. Note that within the GYSELA source code, the electrostatic potential Φ is denoted by the letter U.

In GYSELA all the routines used to solve equations related to the Poisson solver are inside the file `QN_tools.F90`. Hence, 2 subroutines were added within this file: `compute_U_antenna_spatial` and `QN_tools_Compute_U_antenna_and_plasma`. The first calculates the spatial components of the antenna ($S_{ant,1}$ and $S_{ant,2}$ in eq. 4.4), and is called only once on the first iteration, saving $S_{ant,1}$ and $S_{ant,2}$ as global variables. The second subroutine calculates the total antenna potential (eq. 4.4) and adds it to the plasma potential. This subroutine is called at each timestep after the code has calculated, via the routine `QN_tools_solve_3Dsys`, the electrostatic potential of the plasma (so immediately after the step ii) of the Poisson solver explained in sec 2.2.1). Note that the parts of the code that are modified are written in Fortran F90. Here, inside the boxes, are presented all the parts of the code that have been added for integrating the antenna into the code.

In the file `qn_fullkin_elec.F90`, inside the subroutine `QN_FKE_solve`, is called the subroutine `QN_tools_Compute_U_antenna_and_plasma` which compute the Antenna electrostatic potential and add that to the electrostatic potential of the plasma. To switch the antenna on or off, no control is currently created within the input file, so line 327 must be commented out within the `qn_fullkin_elec.F90` file: call `call QN_tools_Compute_U_antenna_and_plasma( self%commons, & timings, Phi)`. This solution needs to be improved and a command needs to be inserted into the input file to switch the antenna on and off.

file: `qn_fullkin_elec.F90`

line 226:

```
    use QN_tools_class, only :    QN_tools_Compute_U_antenna_and_plasma
```

line 327:

```
    call  QN_tools_Compute_U_antenna_and_plasma(self%commons, &
    timings, Phi)
```

The declaration of the variables for the antenna is done inside the file `QN_tools_types.F90`. Here are declared both the spatial parts $S_{ant,1}$ and $S_{ant,2}$, the total electrostatic potential of the antenna U_{ant} and the antenna frequency ω_{ant}.

file: `QN_tools_types.F90`

line 116:

```
    real(F64), dimension(:,:,:), allocatable :: S1_antenna
    real(F64), dimension(:,:,:), allocatable :: S2_antenna
    real(F64), dimension(:,:,:), allocatable :: U_antenna
    real(kind=8), dimension(1) :: antenna_frequency
```

Inside the file `QN_tools.F90` are defined the subroutine `QN_tools_Compute_U_antenna_spatial`, that calculates the spatial part of the antenna (previously declared in file `QN_tools_types.F90`), and the subroutine `compute_U_antenna_and_plasma` that calculate the potential of the antenna and add it to the one of the plasma, giving the total electrostatic potential Φ.

file: `QN_tools.F90`

line 41:

```
    Public:: QN_tools_Compute_U_antenna_and_plasma
```

line 167 (inside the subroutine `QN_tools_init`):

```
    call QN_tools_Compute_U_antenna_spatial(self)
```

line 1908:

```
subroutine QN_tools_Compute_U_antenna_spatial(self)

    use geometry_types
    use MPIutils_mod, only : gstart_Gmapphi, gend_Gmapphi, &
        Gmapping_phi
    use globals, only : Nr, Ntheta, Nphi, minor_radius

    type(QN_tools_t)    , intent(inout) :: self
```

```
    type(geometry_t), pointer :: geom

    ! Declare and initialize arrays for the Antenna Parameters
    integer, parameter :: number_of_mode = 2
    real(F64), dimension(1) :: n = [2.0d0]
    real(F64), dimension(0:number_of_mode-1) :: m_values =
                                                [3.0d0, 4.0d0]
    real(F64), dimension(0:number_of_mode-1) :: a_values =
                                                [0.1d0, 0.1d0]
    real(F64), dimension(0:number_of_mode-1) :: delta_values =
                                                [0.1d0, 0.1d0]
    real(F64), dimension(0:number_of_mode-1) :: s0_values =
                                                [0.5d0, 0.5d0]

    ! Parameter for the construction of the spatial part of the antenna
    integer :: ir, itheta, iphi, m_index
    real(F64), dimension(self%geom_%Nr) :: h_antenna, s
    real(F64) :: angle1, angle2
    real(F64) :: pi_greco

    geom => self%geom_

    MTM_ALLOC_3_ALLOCATABLE( self%S1_antenna, &
        0, geom%Nr-1, 0, geom%Ntheta-1, 0, geom%Nphi-1, 3 )
    self%antenna_frequency = [0.01894d0]
    pi_greco = acos(-1.0d0)
    self%S1_antenna = 0._F64
    self%S2_antenna = 0._F64

    ! Constructing the s array: array from 0 to 1
    do ir = 0, geom%Nr - 1
        s(ir) = geom%rg(ir) / minor_radius
    end do

    if (gstart_Gmapphi.ne. -1 ) then

    ! Do loop for constucting the spatial part of the antenna
       do m_index = 0, number_of_mode-1
           do iphi = gstart_Gmapphi, gend_Gmapphi
              do itheta = 0, geom%Ntheta-1
                 do ir = 0, geom%Nr -2

                    h_antenna(ir) = a_values(m_index) * exp(-(s(ir) - &
```

```
                            s0_values(m_index))**2 /
                            (delta_values(m_index)**2))

                    angle1 = sum(cos(m_values(m_index) *
                            geom%thetag(itheta) + &
                            n * geom%phig(iphi)))

                    self%S1_antenna(ir, itheta, iphi) = &
                           self%S1_antenna(ir, itheta, iphi) &
                            + h_antenna(ir) * angle1

                    angle2 = sum(cos(m_values(m_index) *
                    geom%thetag(itheta) + &
                           n * geom%phig(iphi) + pi_GRECO/2.0))

                    self%S2_antenna(ir, itheta, iphi) = &
                           self%S2_antenna(ir, itheta,iphi) &
                           + h_antenna(ir) * angle2

                 end do
              end do
           end do
       end do
    end if

    end subroutine QN_tools_Compute_U_antenna_spatial
!*********************************************************

subroutine QN_tools_Compute_U_antenna_and_plasma(self, &
        timings, Phi, Siter_time )

    use geometry_types
    use QN_timers_mod, only : QNT_sect_end
    use globals, only :  deltat, Nr, Ntheta, Nphi
    use MPIutils_mod, only : gstart_Gmapphi, gend_Gmapphi, &
        Gmapping_phi

    type(QN_tools_t) , intent(inout) :: self
    type(QN_timers_t), intent(inout) :: timings
    real(F64)        , intent(inout) :: Phi(0:,0:,gstart_Gmapphi:)
    real(F64)        , intent(in)    :: Siter_time

    type(geometry_t), pointer :: geom
```

```
integer :: ir, itheta, iphi

real(F64), dimension(:,:,:), allocatable :: time_S1_antenna
real(F64), dimension(:,:,:), allocatable :: time_S2_antenna

geom => self%geom_

MTM_ALLOC_3_ALLOCATABLE( self%U_antenna, &
    0, geom%Nr-1, 0, geom%Ntheta-1, 0, geom%Nphi-1, 3 )

MTM_ALLOC_3_ALLOCATABLE( time_S1_antenna, &
    0, geom%Nr-1, 0, geom%Ntheta-1, 0, geom%Nphi-1, 3 )

MTM_ALLOC_3_ALLOCATABLE( time_S2_antenna, &
    0, geom%Nr-1, 0, geom%Ntheta-1, 0, geom%Nphi-1, 3 )

time_S1_antenna = 0._F64
time_S2_antenna = 0._F64

!Do loop for constructing the spatial part of the antenna
!and add to the potential of the plasma
if ( gstart_Gmapphi .ne. -1 ) then

   do iphi = gstart_Gmapphi, gend_Gmapphi
     do itheta = 0, geom%Ntheta-1
        do ir = 0, geom%Nr -2
           time_S1_antenna(ir, itheta, iphi) =
                self%S1_antenna(ir, itheta, iphi) &
               * sum(cos(self%antenna_frequency *
                                Siter_time * deltat))

           time_S2_antenna(ir, itheta, iphi) =
                self%S1_antenna(ir, itheta, iphi) &
               * sum(sin(self%antenna_frequency *
                                Siter_time * deltat))

           self%U_antenna(ir, itheta, iphi) = &
               time_S1_antenna(ir, itheta, iphi) + &
               time_S2_antenna(ir, itheta, iphi)

          Phi(ir, itheta, iphi) = Phi(ir, itheta, iphi) + &
               self%U_antenna(ir, itheta, iphi)

        end do
```

```
          end do
       end do

     end if

   end subroutine QN_tools_Compute_U_antenna_and_plasma
```

The parameters that can be changed to modify the antenna are:

- `antenna_frequency`: the frequency of the antenna ω_{ant},
- `n`: the toroidal mode excited by the antenna,
- `number_of_mode`: the number of modes excited by the antenna (in our case is two),
- `m_values`: the poloidal mode m_j excited by the antenna,
- `a_values`: the amplitude of the perturbation a_j (eq. 4.2),
- `delta_values`: the variance δ_j of the radial gaussian profile (eq. 4.2),
- `s0_values`: the mean of the Gaussian radial profile $r_{0,j}$ (eq. 4.2).

In view of future developments, these parameters should be placed in the input file of GYSELA, so that they can be changed without modifying the code.
As can be seen from the equation 4.4, the electrostatic potential of the antenna needs the time variable t. In GYSELA, the teration is provided by the variable `Siter_time` defined in the file `vlasov/boltzmann_solving.F90` in the subroutine `BLZ_predcorr`. The time t to be inserted within the equation (and thus within the code) is obtained by multiplying `Siter_time` by the timestep dt. In order to insert the variable `Siter_time` within the subroutine `QN_tools_Compute_U_antenna_and_plasma`, the following changes, highlighted in red, were made within various files:

Modification for adding the time of the iteration

- File `gysela.F90`:
  line 234:
  `call BLZ_predcorr_step0( boltz, iter_time, em_field3D, pfnp1, fequil4d, potential, magnetic_potential )`
- File `valsov/boltzmann_solving.F90`:
  line 288:
  `subroutine BLZ_predcorr_step0( self, Siter_time, em_field3D, fnp1, fequil4d, potential, magnetic_potential )`
  - line 300:
    `real(F64), intent(in) :: Siter_time`
  - line 388:
    `call QN_solver_solve( poiss, J0, fnp1, fequil4d, potential, Siter_time )`
  - line 600:
    `call QN_solver_solve( poiss, J0, fnp1, fequil4d, potential, Siter_time)`
- File `poisson/qn_solver.F90`:
  line 223:
  `subroutine QN_solver_solve( self, J0, f, fequil4d, potential, Siter_time )`
  - line 242:
    `real(F64) , intent(in) :: Siter_time`
  - line 259: `call QN_FKE_solve( self, J0, f, fequil4d, potential, Siter_time )`
- File `poisson/ qn_fullkin_elec.F90`:
  line 255:
  `subroutine QN_FKE_solve( self, J0, f, fequil4d, potential, Siter_time )`
  - line 279:
    `real(F64) , intent(in) :: Siter_time`
  - line 281:
    `call QN_tools_Compute_U_antenna_and_plasma(self%commons, timings, Phi, Siter_time)`

All these changes were saved in GYSELA's GitHub, in the branch: "`LB_electorstatic_antenna`"

Before studying the effects the antenna has on the plasma, preliminary studies were carried out to see if the antenna was implemented correctly within the code. As can be seen by comparing the figure 4.2 obtained by plotting the theoretical equation and the figure 4.4 obtained by post-processing analysis with the script of python routines available in GYSELA, the antenna was implemented correctly. Furthermore, inside the subroutine `QN_tools_Compute_U_antenna_spatial` were changed the antenna parameters (i.e. $r_{0,j}$, δ_j and a_j from eq. 4.2), thus changing the shape of the antenna. The theoretical results were compared with the output obtained by post-processing the GYSELA data, finding a variation as predicted. More specifically, changing the mean of the Gaussian $r_{0,j}$ resulted in a different centering of the radial peak, changing the variance δ_j resulted in a change in the width of the distribution, and changing the amplitude a_j resulted in a change in the amplitude from the output data of the electrostatic potential computed by GYSELA.

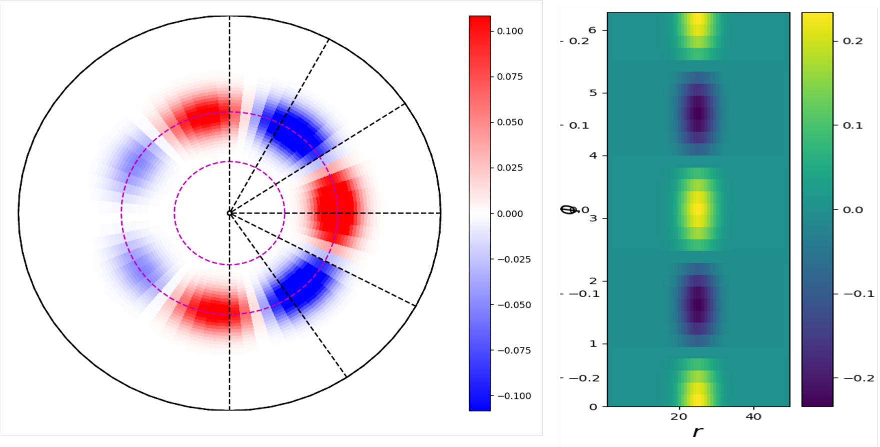

Figure 4.4: *Poloidal (left) and toroidal (right) cross-section of the electrostatic antenna* Φ_{ant} *at* $t = 0$ *obtained after the implementation in GYSELA. To note that is the same as the theoretical prediction shown in fig. 4.2, hence the antenna is correctly implemented within GYSELA.*

4.3 Effects of the antenna on the plasma

After testing the correct implementation of the antenna within the code, the effects that this antenna has on the behaviour of the plasma were analysed. It is important to emphasise that all these results are preliminary and further studies need to be performed to fully understand how the interaction between the antenna and the plasma takes place.

4.3.1 Simulations parameters

For all the simulations in which the antenna is implemented, it was used a flat profile for density and temperature, a mass ratio $m_i/m_e = 200$, $\beta = 9.1 \times 10^{-4}$, $\rho^* = 1/50$, a spatial resolution $(N_r, N_\theta, N_\varphi) = (64, 64, 32)$ and time step $dt = 1\omega_{c0}^{-1}$. The q profile used for the simulation is the same as the reference case 'ITPA-TAE' [27]: $q = 1.71 + 0.16r^2$. With these parameters, the frequency of the TAE is $\omega_{TAE\ gap} = 1.894 \times 10^{-2}\omega_{c0}$. Figure 4.5 represents the Alfvén continua resulting from the parameters used in these simulations.

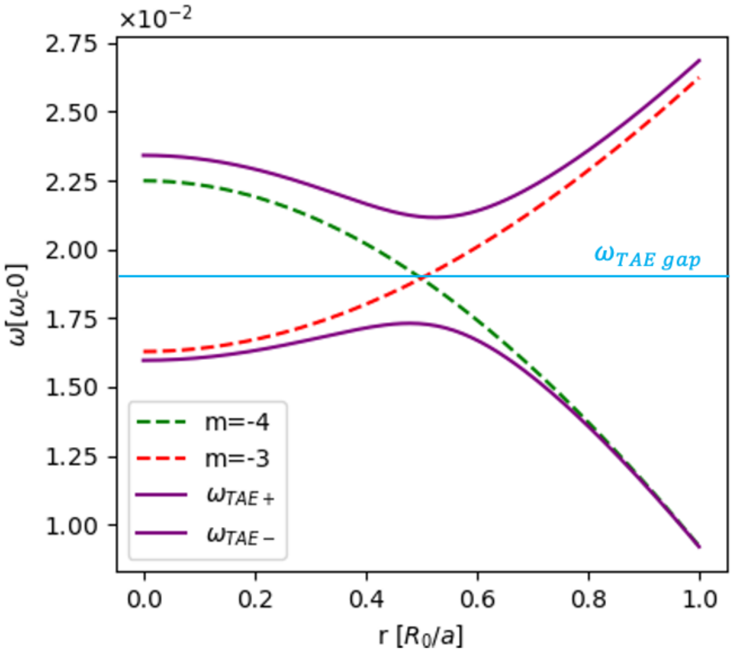

Figure 4.5: *Alfvén continua of the simulations where the antenna is implemented for* $n = 2$ *and* $m = -3$ *and* $m = -4$. *It is possible to see the TAE gap due to the coupling between this mode. In blue, it highlights the frequency of the center of the gap, referred as* $\omega_{TAE\ gap}$

GYSELA exploits the invariance of μ (described in section 1.2.6), thus μ thus assumes the role of a parameter. In particular, within the code, for each species, the Boltzmann equations are calculated independently for each value of μ. The values of calculated μ are defined in the input file by the parameters `mumin`, `Lmu` and `Nproc_mu`, these are respectively the minimum value of μ (set to zero in these simulations), the maximum value of μ ($= 32$ in these simulations) and the number of processors used to compute μ. The latter in particular refers to the number of μ values that are calculated. In these simulations (as in all simulations involving magnetic effects in GYSELA) `Nproc_mu` $= 32$. This means that the dynamics are evaluated for 32 values of μ. This value is very important because changing the value of `Nproc_mu` gives very different results. This leads to a large increase in the computational cost since at least 32 nodes need to be used for each simulation. That is a constraint that concerns only simulations carried out with electromagnetic effects.

In the following part of this chapter, we are going to present some results obtained by implementing the antenna in GYSELA.

4.3.2 Results of the simulations with the antenna

As a first study, the antenna was inserted from the beginning of the simulation (so at $t = 0$) with a frequency equal to that of the center of the gap ($\omega = 1.894 \times 10^{-2}\omega_{c0}$ see fig. 4.5) with amplitude $a = 0.1$, the same used by *Sadr et al.* [30].

Figure 4.6 shows the 8 modes with greater amplitude for the electrostatic potential Φ(top panel) and for the parallel component of the magnetic vector potential $A_{\|}$ (bottom panel). This analysis consider the 8 most energetic modes at a given time (in all the results presented here, the time chosen is the time at the end of the analysis, i.e. in figure 4.6, the 8 most energetic modes are calculated at $t = 10000/\omega_{c0}$) and plots the absolute value of Φ and $A_{\|}$ for these modes over time. As can be seen, although the antenna was only inserted in the electrostatic potential, there are also effects in the magnetic part. In more details, it is possible to observe how there is an initial damping of the perturbed modes ($m = -3$ and $m = -4$, in blue and red respectively for Φ and vice-versa for $A_{\|}$), reaching a saturation value of $\Phi \sim 10^{-2}$ and $A_{\|} \sim 10^{-4}$. The modes perturbed by the antenna have energy one order of magnitude higher than all the others, both in Φ and in $A_{\|}$. Analyzing the poloidal section (figure 4.7) it is evident that the antenna is the dominant part in both Φ (left) and $A_{\|}$ (right), as can be seen by the peak of greatest amplitude centred in the middle of the radial domain. Furthermore, there is a radial redistribution of energy, particularly evident in Φ, where perturbations can be observed both internally and externally to the central peak.

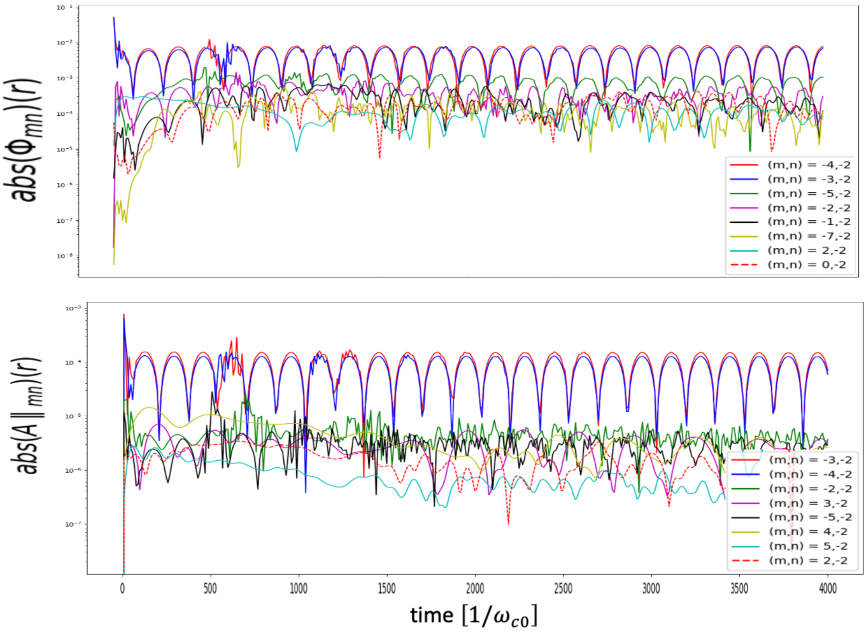

Figure 4.6: *Eight most energetic modes of Φ (above) and $A_{\|}$ (belove) in the case where the antenna is inserted from the beginning of the simulation (at $t = 0$). The perturbed modes ($m = -3$ and $m = -4$ are in blue and red respectively for Φ and vice-versa for $A_{\|}$. It is clear that these 2 modes have an initial damping and saturation values one order of magnitude higher than the other modes.*

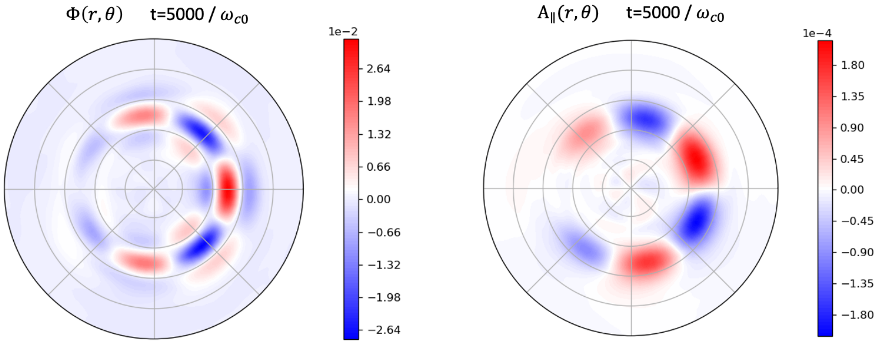

Figure 4.7: *Poloidal section of Φ (left) and $A_{\parallel}$ (right) in the case where the antenna is inserted from the beginning of the simulation (at $t = 0$). The central peak due to the antenna is clearly visible and a radial redistribution of energy is observed.*

Some preliminary studies on the distribution function were also carried out. In these simulations, only the 2D distribution function of hydrogen was saved and analysed, dependent only on $v_{\perp}$ and $v_{\parallel}$, calculated at $r/a = 0.5,\ \theta = 0,\ \varphi = 0$. These values were not chosen but are the ones GYSELA uses when saving the 2D distribution function. Figure 4.8 shows the distribution function for values of $v_{\perp}/v_{th} = 0$, i.e. for $\mu = 0$, at the beginning of the simulation ($t = 0/\omega_{c0}$) (top pannel) and at time $t = 10000/\omega_{c0}$ (bottom panel). v_{th} is the thermal velocity of the ions and is used as the normalization velocity in GYSELA. It can be seen that, following the introduction of the antenna, a perturbation appears at higher energies (highlighted by the grey circles). This is a positive indication, as we are going to insert a perturbation that interacts in a similar way as fast ions. However, to gain a clearer understanding of the phenomenon, further studies are needed, also analysing the 5D distribution function. In GYSELA it is possible to save the outputs of the 5D distribution function, but such analysis was not carried out due to lack of time.

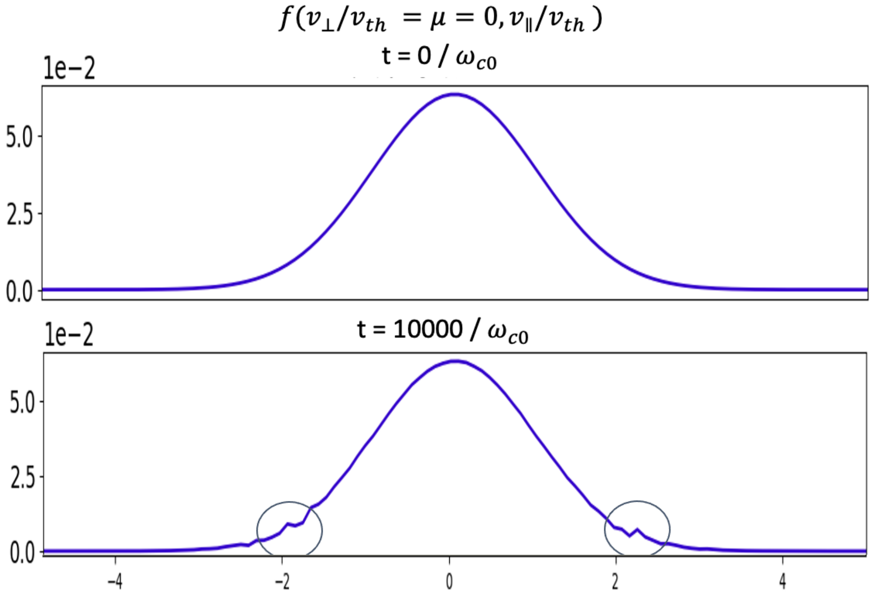

Figure 4.8: *2D distribution function of hydrogen at* $t = 0/\omega_{c0}$ *(above) and at* $t = 10000/\omega_{c0}$ *(belove) in the simulation with the antenna inserted since the beginning. It is possible to observe the presence of a peak at higher energies (highlighted by the grey circles) following the introduction of the antenna.*

Amplitude and frequency studies were carried out to understand better the plasma response in this configuration. In particular, simulations were done with the same frequency of the antenna and amplitude 10 times smaller (a = 0.01) and 100 times smaller (a =0.001) than the case just shown. In both of these cases, differences were observed in the amplitude of the oscillations, as expected as the parameter was changed, but no substantial differences in frequencies and patterns with respect to the previous one. Regarding the frequency studies, were performed simulations with frequency 10 times smaller ($\omega_{ant} = 1.894 \times 10^{-3}\omega_{c0}$) and 10 times larger ($\omega_{ant} = 1.894 \times 10^{-1}\omega_{c0}$) with respect to the one of the center of the gap. Regarding the first one, a difference in the frequencies of the oscillations was observed, but the behaviour was the same as in the case with the same frequency as the centre gap. This contrasts with theoretical predictions, since by placing a perturbation with frequency crossing the continuum, this should be damped. However, this is not observed. In the latter, there was a problem regarding the saving of the data. The timestep used has always been $dt = 1\omega_{c0}^{-1}$, but data were saved every 10 timesteps for computational reasons, (both to save data less frequently and to have lighter and more manageable output files to analyze). This allows frequencies up to 10^{-1} ω_{c0} to be studied. In all the previous cases, all phenomena studied had lower frequencies, so they could be studied since more data for each period are saved, and thus available for the post-process analysis. Going to study frequencies in the order of $10^{-1}\omega_{c0}$, saving data every 10 timesteps is no longer suitable and one needs to save data more frequently. So the results obtained with this frequency were not useful for the analysis. To better understand the behaviour of the plasma as the antenna frequency varies, further studies need to be carried out by modifying the antenna frequency and analysing the plasma response.

For further studies, the antenna and simulation parameters were left unchanged, but the antenna was inserted at $t = 68000/\omega_{c0}$ and not from the beginning of the simulation. Clear differences were observed between these two simulations. In figure 4.9 the 8 modes are shown with greater amplitude of Φ. As can be seen, Immediately after the introduction of the antenna, there is a simultaneous growth of all modes and, once the saturation regime is reached, all modes have about the same energy (~ 1) which is one order of magnitude higher than in the case where the antenna was inserted from the beginning. The presence of multiple modes with the same energy can be observed clearly in the poloidal section of the electrostatic potential shown in figure 4.10. From these, it is not possible to observe the presence of a clear predominant mode over the others. Also, peaks are observed near the edges of the domain, this is a potential indicator of problems due to boundary conditions in GYSELA (as explained in section 3.2).
The difference between these two simulations must be studied, as such diverse behaviour was not predicted by inserting the perturbation at the beginning or during the simulation. A difference can be expected when the antenna is introduced, but once saturation is reached, the amplitude and characteristics of the various modes should be the same

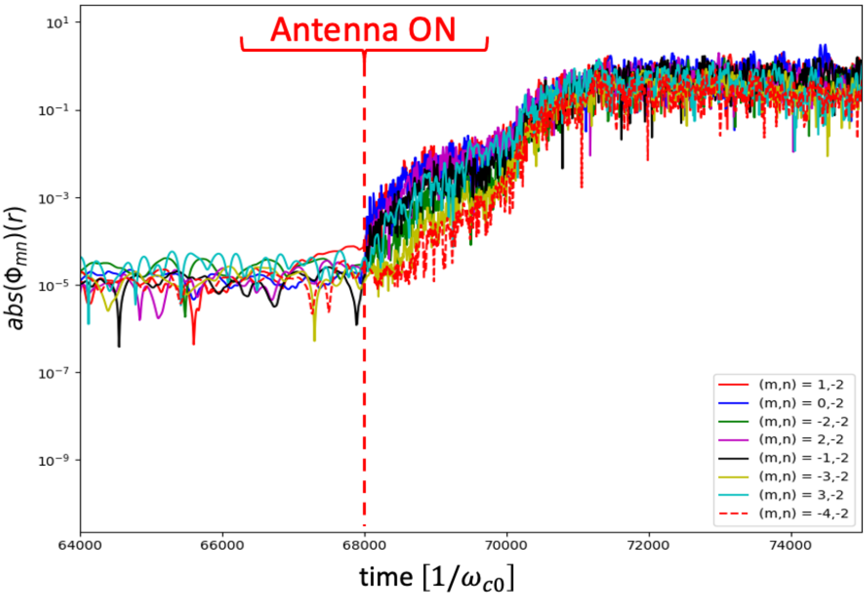

Figure 4.9: *Eight modes with greater amplitude of Φ, with the antenna turned ON during the simulation. Simultaneous growth of all modes is observed once the antenna is inserted and once saturation is reached all modes have the same energy.*

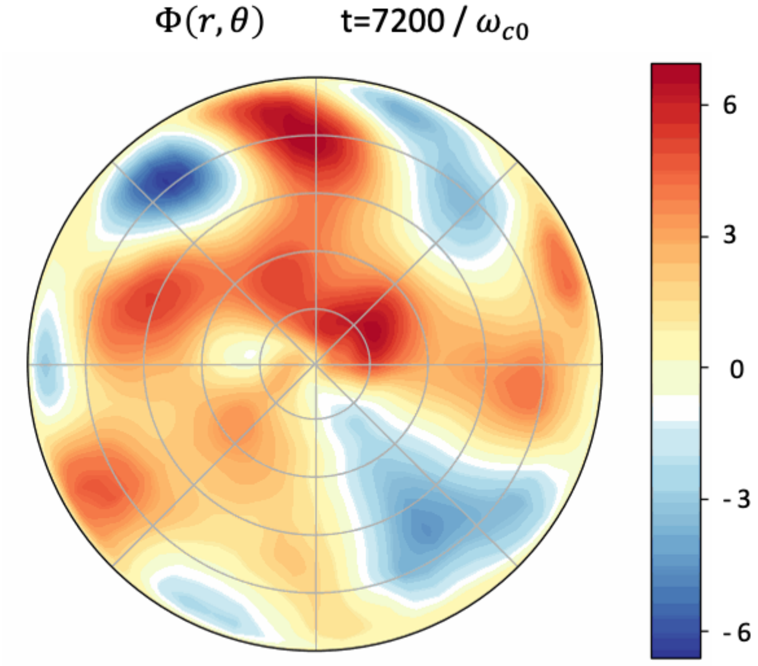

Figure 4.10: *Poloidal section at* $t = 72000/\omega_{c0}$*, thus after the plasma has reached the saturation level, in the case where the antenna is inserted during the simulation. It is not possible to observe the presence of a clear predominant mode over the others. Note the difference with the case where the antenna was inserted at the beginning of the simulation (fig. 4.7).*

These preliminary results differ from the results presented in the reference case 'ITPA-TAE' [27] and in [30]. Moreover, we expect the perturbed modes to grow more and to have higher energy than the non-perturbed modes. This latter point is clearly visible in the case where we insert the antenna from the beginning (fig. 4.7). However, we have a damping of the perturbed modes (fig. 4.6) and not a growth as observed in the literature. In the case in which we insert the antenna once the simulation is already started, we have a growth of the modes that are more similar to the phenomenon present in literature. However, all the modes grow simultaneously at the same rate (fig. 4.9), without observing any difference between the perturbed and non-perturbed modes.
To further understand the phenomenon, studies on the growth rate must be carried out to see if the growth is comparable with the one observed in the literature.
In addition, it must be studied in more detail why these differences are present. These, in part, may also be due to how the electromagnetic part is implemented in GYSELA. Being a newly implemented part, it is also necessary to understand the right parameters to use for a more in-depth and detailed study of this phenomenon.

An additional simulation was carried out exciting through the antenna the $m = -1$ and $m = -2$ modes, thus perturbing the modes for which the gap in the continuum is close. All other parameters, of the antenna and the simulation, were left unchanged. The frequency of the antenna was also not changed ($\omega_{ant} = 1.894 \times 10^{-2}$) and the antenna is inserted at the beginning of the simulation (at $t = 0$). In figure 4.11 the continuum for the simulation parameters is shown. It can be seen that the $m = -1$ and $m = -2$ modes do not overlap and open these gap in the continuum, so we will expect that such a perturbation will be damped by the continuum. However, from observing the 8 modes with greater amplitude of Φ (fig. 4.12) there are no substantial differences from the case in which the antenna excited the modes $m = -3$ and $m = -4$ with the same frequency (fig. 4.6). In particular, an initial damping of the excited modes is also observed in this case, and once stabilized these modes have a value of $\Phi = 10^{-1}$ and have more energy than the others.

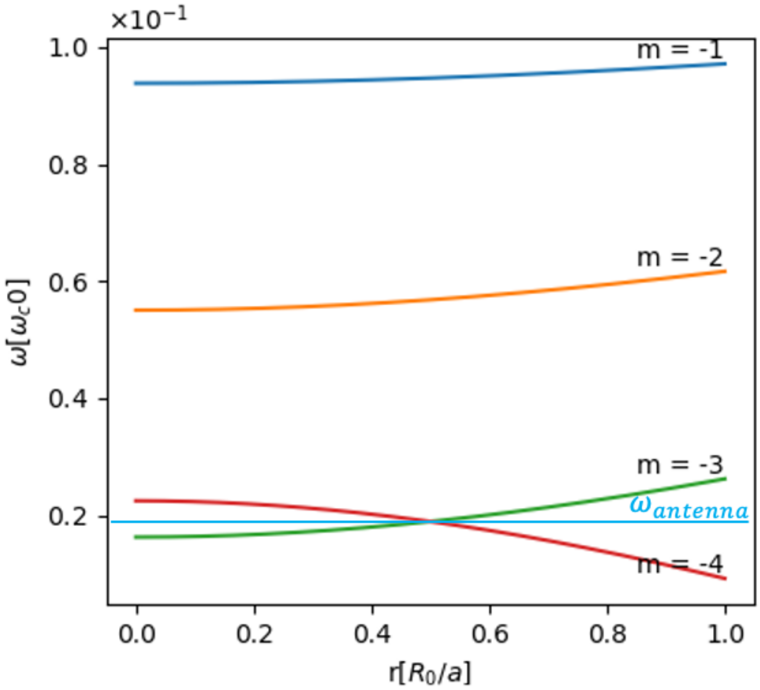

Figure 4.11: *Alfvén continua of the case where the antenna was implemented for* $n = 2$ *and* $m = -1, -2, -3, -4$.

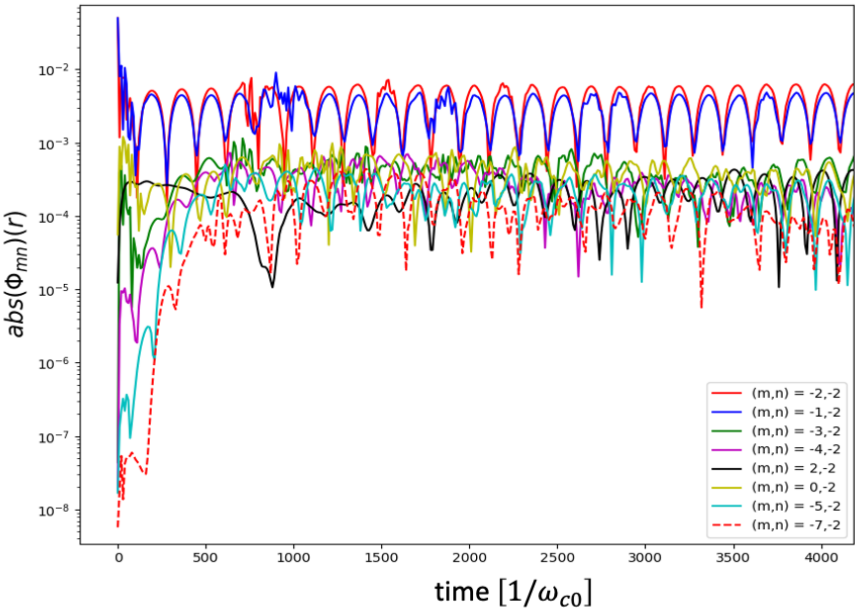

Figure 4.12: *Eight most energetic modes of Φ in the case where the antenna is inserted from the beginning of the simulation (at $t = 0$). The perturbed modes ($m = -1$ and $m = -2$ are in blue and red respectively. These 2 modes have initial damping and saturation values one order of magnitude higher than the other modes. No substantial difference is observed from the case where the antenna perturbs the modes ($m = -3$ and $m = -4$ (fig. 4.6).*

In this section, it has been shown that the plasma reacts, both for the electrostatic and electromagnetic parts, to an electrostatic antenna. The antenna we inserted is intended to excite the modes within the gap in the continuum, thus not subject to damping, so a growth of the perturbed modes was expected. This was not always observed because initial damping was observed in simulations where the antenna was inserted from the beginning. Further studies are needed to understand what this damping is due to. In addition, inserting the antenna while the simulation has already started results in a different plasma response, with a growth of all the modes. So we have shown that the plasma reacts to the insertion of the antenna, even if it is still unclear whether we are observing the excitation of TAEs.

Chapter 5

Conclusion

This work pursued the goal of studying the phenomena of the interaction between the Alfvén waves and the plasma using GYSELA.

The initial part of the work has been devoted to study the Alfvén Eigenmode in a cylindrical configuration. Specifically, a perturbation was initialized with a defined value of poloidal mode number m and a toroidal mode number n. These simulations were carried out using a flat q profile and performing a scan through various values of the safety factor q. We measured the frequency of the oscillation of the electrostatic potential Φ and of the parallel component of the vector potential $A_{\parallel}$ through a Fourier analysis. We observed what was expected from the theory: a clear damping with the dominant frequency which was the same as that predicted for Shear Alfvén waves. So, we conclude that GYSELA can contemplate the continuum existence.

After having performed studies in a cylindrical configuration, a more realistic toroidal configuration was analysed, using the same parameters of the cylindrical configuration, but changing the aspect ratio. With the decreasing of the aspect ratio, we could not observe anymore a clear dominant structure and there was no dominating damping frequency. An analysis of the poloidal section of Φ revealed the presence of the predominant modes near the boundaries, which can be an indicator of the boundary issues: the electrostatic potential in the outer boundary satisfies Dirichlet's conditions, so it is set equal to zero. This choice (studied and well-established in the code) may affect the plasma in the immediate proximity of this boundary. Furthermore, simulations were performed with increasing the domain, resolution and change of the q profile, using a parabolic q profile and investigating perturbations on different modes. Even with these changes, it was not possible to observe the gap present in the continuum.

Thus, after investigating the behaviour of the plasma following an initial perturbation, we proceeded to excite the modes present in the continuum gap through an external electrostatic antenna. After having implemented the electrostatic antenna inside GYSELA, simulations were carried out to ensure the robustness and consistency of these modifications. Once it was confirmed that the antenna behaved as expected, the analysis proceeded to examine the plasma's response to this antenna perturbation. To do this, analyses were done on varying different parameters such as frequency, amplitude and modes excited by the antenna. It was observed how the plasma changes its response as a result of the modification of the parameters. The obtained results diffear from the predicted theoretical results and also exhibit differences depending on whether the antenna is inserted from the beginning or during the simulation. This should not happen since differences can be expected as soon as the antenna is introduced, but once at a steady state, the plasma behaviour is expected to be the same. These differences need to be the subject of further and more in-depth studies.

The results obtained are only preliminary and further studies are needed to gain a physical and numerical understanding of the phenomenon in GYSELA. Further studies can be done by tuning and scanning the parameters to identify the best one to operate in GYSELA. Studies can also be carried out by analyzing the distribution function and finally adding the antenna to the magnetic part to have a better understanding of this phenomenon.

In conclusion, the thesis showed interesting results in the study of TAEs in GYSELA and laid the foundation for the study of the interaction between TAEs and turbulence with GYSELA, a topic of fundamental importance in view of future fusion reactors.

References

[1] Alinka Lépine-Szily et al. “Nuclear astrophysics: nucleosynthesis in the Universe”. In: *International journal of astrobiology* 11.4 (2012), pp. 243–250.

[2] Jef Ongena. “Fusion: A true challenge for an enormous reward”. In: *EPJ Web of Conferences*. Vol. 189. EDP Sciences. 2018, p. 00015.

[3] M. Schirber. “Gaining ground in nuclear fusion”. In: *Physics* 15.195 (2022).

[4] Francis Chen. *Introduction to Plasma Physics and Controlled Fusion*. Springer, 1974.

[5] John Wesson et al. *Tokamaks*. Vol. 149. Oxford university press, 2011.

[6] Thomas James Morrow Boyd et al. *The physics of plasmas*. Cambridge university press, 2003.

[7] Dani Irawan et al. “Modeling and characterization of charged particle trajectories in an oscillating magnetic field”. In: *AIP Conference Proceedings*. Vol. 1656. 1. AIP Publishing. 2015.

[8] Liu Chen et al. “Plasma heating by spatial resonance of Alfvén wave”. In: *The Physics of Fluids* 17.7 (1974), pp. 1399–1403.

[9] Linjin Zheng. “Gyrokinetic theory”. In: *Advanced Tokamak Stability Theory*. 2053-2571. Type: Book Chapter. Morgan & Claypool Publishers, 2015, 4–1 to 4–36.

[10] Alain J Brizard et al. “Foundations of nonlinear gyrokinetic theory”. In: *Reviews of modern physics* 79.2 (2007), p. 421.

[11] Xavier Garbet et al. “Neoclassical equilibrium in gyrokinetic simulations”. In: *Physics of Plasmas* 16.6 (2009).

[12] Virginie Grandgirard et al. “Gyrokinetic simulations of magnetic fusion plasmas”. In: *Panoramas et syntheses (39-40)* (2013), pp. 91–176.

[13] FL Hinton et al. “Theory of plasma transport in toroidal confinement systems”. In: *Reviews of Modern Physics* 48.2 (1976), p. 239.

[14] Samuele Mazzi. “Impact of fast ions on microturbulence in fusion plasmas”. PhD thesis. Aix-Marseille Université, 2021.

[15] WW Heidbrink et al. “The behaviour of fast ions in tokamak experiments”. In: *Nuclear Fusion* 34.4 (1994), p. 535.

[16] Liu Chen et al. “Physics of Alfvén waves and energetic particles in burning plasmas”. In: *Reviews of Modern Physics* 88.1 (2016), p. 015008.

[17] W. W. Heidbrink. “Basic physics of Alfvén instabilities driven by energetic particles in toroidally confined plasmas”. In: *Physics of Plasmas* 15.5 (Feb. 2008), p. 055501.

[18] Fulvio Zonca et al. “Theory of continuum damping of toroidal Alfvén eigenmodes in finite- tokamaks”. In: *Physics of Fluids B: Plasma Physics* 5.10 (Oct. 1993), pp. 3668–3690.

[19] Hannes Alfvén. “Existence of electromagnetic-hydrodynamic waves”. In: *Nature* 150.3805 (1942), pp. 405–406.

[20] GY Fu et al. “Excitation of the toroidicity-induced shear Alfvén eigenmode by fusion alpha particles in an ignited tokamak”. In: *Physics of Fluids B: Plasma Physics* 1.10 (1989), pp. 1949–1952.

[21] TH Stix. “Waves in Plasmas, American Inst”. In: *Physics, New York* (1992), p. 86.

[22] A Fasoli et al. “Alfvén eigenmode experiments in tokamaks and stellarators”. In: *Plasma Physics and Controlled Fusion* 39.12B (1997), B287.

[23] M Garcıa-Muñoz et al. “Convective and diffusive energetic particle losses induced by Shear Alfvén waves in the ASDEX Upgrade tokamak”. In: *Physical review letters* 104.18 (2010), p. 185002.

[24] Virginie Grandgirard et al. “A 5D gyrokinetic full-f global semi-lagrangian code for flux-driven ion turbulence simulations”. In: *Computer Physics Communications* 207 (2016), pp. 35–68.

[25] Camille Gillot. “Model reduction for tokamak plasma turbulence : beyond fluid and quasi-linear descriptions”. Theses. Aix Marseille Université, Dec. 2020.

[26] Bigue Romeo. *Magnetic reconnection mechanisms for the tearing instability.* 2023.

[27] Axel Könies et al. “Benchmark of gyrokinetic, kinetic MHD and gyrofluid codes for the linear calculation of fast particle driven TAE dynamics”. In: *Nuclear Fusion* 58.12 (2018), p. 126027.

[28] Wenlu Zhang et al. “Global gyrokinetic particle simulation of toroidal Alfvén eigenmodes excited by antenna and fast ions”. In: *Physics of Plasmas* 19.2 (Feb. 2012), p. 022507.

[29] A. Biancalani et al. “Linear gyrokinetic particle-in-cell simulations of Alfvén instabilities in tokamaks”. In: *Physics of Plasmas* 23.1 (Jan. 2016), p. 012108.

[30] Mohsen Sadr et al. “Linear and nonlinear excitation of TAE modes by external electromagnetic perturbations using ORB5”. In: *Plasma Physics and Controlled Fusion* 64.8 (July 2022), p. 085010.

[31] Zhihong Lin et al. “Turbulent transport reduction by zonal flows: Massively parallel simulations”. In: *Science* 281.5384 (1998), pp. 1835–1837.

[32] Ben F McMillan et al. “Long global gyrokinetic simulations: Source terms and particle noise control”. In: *Physics of Plasmas* 15.5 (2008).

[33] V. Aslanyan et al. “Gyrokinetic simulations of toroidal Alfvén eigenmodes excited by energetic ions and external antennas on the Joint European Torus”. In: *Nuclear Fusion* 59.2 (Dec. 2018), p. 026008.

[34] Theodore Panis et al. “Optimization of the active MHD spectroscopy system on JET for the excitation of individual intermediate and high-n Alfvén eigenmodes”. In: *Nuclear Fusion* 50.8 (2010), p. 084019.

[35] P Puglia et al. “The upgraded JET toroidal Alfvén eigenmode diagnostic system”. In: *Nuclear fusion* 56.11 (2016), p. 112020.

[36] Roy Alexander Tinguely et al. “A novel measurement of marginal Alfvén eigenmode stability during high power auxiliary heating in JET”. In: *Nuclear Fusion* 62.7 (2022), p. 076001.